Technical University of Munich
Ludwig-Maximilians-University Munich
Department of Physics
Chair of Solid-State Theory

Measurement-induced entanglement transitions in random qudit circuits

Aamod Vinayak Atre

Thesis submitted within the Master's Program
Quantum Science & Technology

May 08, 2025

Supervisors:
Prof. Dr. Frank Pollmann
Raúl Morral-Yepes

First Examiner: Prof. Dr. Frank Pollmann
Second Examiner: Prof. Dr. Michael Knap

Technische Universität München
Ludwig-Maximilians-Universität München
Fakultät für Physik
Lehrstuhl für Theoretische Festkörperphysik

Messung-induzierte Verschränkungsübergänge in zufälligen Qudit-Schaltkreisen

---

Aamod Vinayak Atre

Abschlussarbeit im Masterstudiengang
Quantum Science & Technology

08. Mai 2025

Betreuer:
Prof. Dr. Frank Pollmann
Raúl Morral-Yepes

Erstgutachter: Prof. Dr. Frank Pollmann
Zweitgutachter: Prof. Dr. Michael Knap

ABSTRACT

Random quantum circuits provide a framework for probing universal dynamical phenomena in chaotic quantum many-body systems, by circumventing the microscopic details of Hamiltonian evolution. Bipartite entanglement measures can be used to characterize the dynamical phases that emerge in these systems. Typically, under random unitary evolution, bipartite entanglement entropies exhibit a linear growth, and attain steady-state values that scale extensively with the system volume. However, when local projective measurements are introduced, a suppression of steady-state bipartite entropies occurs, leading to a subextensive scaling with the system volume. This class of entanglement scaling transitions, from an extensive to a sub-extensive scaling regime, has sparked interest in a broader class of measurement-induced phase transitions, with a potential to further our understanding of fault-tolerance in quantum computing, and in realizing synthetic quantum phases on digital quantum simulators. In this work, we characterize entanglement scaling transitions in one-dimensional random quantum circuits composed of q-level systems, with the local Hilbert space dimension $q \geq 2$. This predominantly numerical study employs generalizations of the stabilizer formalism and the Clifford group to higher-dimensional Hilbert spaces to simulate the measurement-induced transitions. We find that the nature of the entanglement scaling transition remains invariant under changes in the local Hilbert space dimension. However, the critical measurement rate inducing the transition increases with q, asymptotically approaching $1/2$ in the limit $q \to \infty$. To further explore this classical limit, we develop a minimal dynamical model that captures entanglement structures under unitary evolution. We analyze the entanglement structures in thermal stabilizer states using this model, and propose an approach for incorporating measurements within this framework.

Contents

Chapter 1

Introduction

Quantum entanglement is a fundamental phenomenon in quantum physics, describing the intrinsic non-classical correlations shared between subsystems of a composite quantum state. In entangled systems, the state of each particle cannot be described independently of the others, regardless of their spatial separation. Historically, this counterintuitive behavior challenged classical notions of locality and realism, and raised skepticism towards the completeness of quantum mechanics. These concerns were notably articulated in the Einstein-Podolsky-Rosen (EPR) paradox in 1935 [1]. Subsequently, Bell's formulation of mathematical bounds on classical correlations, dubbed as Bell's inequalities, sought to relieve this discrepancy between classical intuitions and quantum correlations [2]. An experimental violation of these inequalities thus provided a clear test of the non-locality of quantum correlations. Consequently, over the past decades, successive experiments [3–7] have confirmed these violations, with an increasing confidence that key theoretical loopholes were closed, and hence, the non-local nature of quantum entanglement was empirically verified.

Despite bearing deep mathematical roots, entanglement now plays a central role as a resource in quantum information science. It underpins a wide array of applications including: quantum algorithms and error-correcting codes [8–10]; quantum communication protocols such as teleportation and entanglement swapping [11, 12]; secure quantum key distribution [13]; and enhanced measurement precision in quantum sensing and metrology [14–16].

In modern condensed matter physics, entanglement has been instrumental in characterizing quantum many-body states. The scaling of entanglement entropy near quantum critical points exhibits universal features that offer insight into the conformal field theories governing such transitions [17, 18]. Entanglement also plays a role in identifying topologically ordered phases, either through measures such as the topological entanglement entropy [19] or via the structure of the entanglement spectrum [20]. Moreover, the study of entanglement has influenced the development of efficient numerical techniques, such as tensor network methods [21, 22], whose accuracy depends on the low entanglement of the many-body wavefunction [23–25]. Entanglement measures are also instrumental in probing non-ergodic phenomena, such as many-body localization [26, 27], where the entanglement growth and saturation differ from those observed in non-integrable thermalizing systems.

Recent experimental advances in quantum simulation have motivated a new interest in studying entanglement dynamics in non-equilibrium systems. Contemporary quantum hardware platforms typically operate with an elementary set of operations: local and two-qubit unitary gates, local projective measurements, and mid-circuit feedback loops dependent on the measurement outcomes [28]. Multi-qubit unitary operations generically lead to delocalization of quantum information. This *information scrambling* promotes entanglement growth and thermalization in many-body systems, while projective measurements act to locally collapse wavefunctions and reduce entanglement. This competing behavior has shown

to give rise to distinct phases of steady state entanglement [29]. At a low proportion of measurement operations, systems exhibit an extensive entanglement scaling with their size, while a higher proportion of measurements yields sub-extensive entanglement scaling. This dynamical phase transition between entanglement scaling phases, driven by the frequency of measurements, is denoted as a measurement-induced phase transition (MIPT).

While random quantum circuits were originally employed for demonstrating quantum computational advantage [30], they have become a playground to explore and analyze MIPTs. The typical model of a random quantum circuit is composed of two-qubit unitary gates arranged in a brickwork pattern. In such models, these circuits exhibit three primary sources of randomness: the unitary gates are sampled uniformly from the unitary group $U(4)$, the measurement locations are determined probabilistically, and measurement outcomes are inherently probabilistic due to the Born rule. Thus, entanglement dynamics are studied by ensemble averaging over many circuit realizations. The measurement rate emerges as the sole tunable parameter driving the phase transition. Extensive studies have characterized MIPTs appearing across various circuit models: in one-dimensional Haar-random [31, 32] and Floquet systems [29], in measurement-only circuits [33], in fine-tuned unitary-only circuits [34], in higher spatial dimensions [35], and with joint measurements to realize symmetry-protected topological order [36].

To date, most studies of MIPTs have focused on qubit systems. This is natural, as the discourse on modern quantum technolgies is generally qubit-centric, following the binary nature of classical computing. However, interest has been growing in systems with local Hilbert space dimension $q > 2$, i.e., qudits [31, 32, 37–43]. Qudit-based quantum protocols carry structural advantages which offer resource efficiency and experimental versatility, raising the question of how entanglement dynamics and MIPTs manifest in higher-dimensional local Hilbert spaces.

A key structural advantage of qudits is their ability to represent large Hilbert spaces more compactly. To encode an L-particle system, only $n_q = \log_q L$ qudits are needed, compared to $\log_2 L$ qubits. Foundational quantum algorithms, such as the oracle-based Deutsch-Jozsa and Bernstein-Vazirani algorithms, Grover's search, and the quantum Fourier transform, have natural generalizations to higher dimensions [44, 45]. Certain error-correcting codes have shown improved thresholds and efficiency with increasing qudit-dimension [46], while quantum communication using higher-dimensional encodings promise a greater resilience to environmental noise and eavesdropping [47]. Furthermore, qudits naturally encode a broad class of physical systems, including molecules with non-adiabatic dynamics or extensive vibrational modes [48, 49], multi-mode light-matter interactions [50], and lattice gauge theories [51]. Variational quantum algorithms such as the quantum approximate optimization algorithm (QAOA) also benefit from flexible local Hilbert spaces [52]. Another distinct advantage of qudits is their ability to embed qubit operations within their larger Hilbert spaces. Embedding can enable reductions in circuit depth by replacing two-qubit gates with single-qudit operations [53]. Thus, circuit complexity can be reduced for obtaining arbitrary unitaries, performing generalized measurements [54], and consequently algorithms [55]. Additionally, embedding also provides an avenue for efficient error correction protocols [56–58].

Although still relatively sparser than qubit systems, qudit architectures have been realized experimentally. Photonic platforms have supported qutrits on multiple degrees of freedom such as orbital angular momentum, frequency bins, and time bins [45]. Realizations on trapped-ion systems have demonstrated universal gate sets for qudits up to dimension

$q = 7$ [59, 60]. Superconducting setups have also been explored in higher dimensions [61]. The experimental generalizations of qubit platforms come with their share of engineering challenges: such as increased cross-talk among the qudit levels and noisy readouts with increasing level density.

In this thesis, we investigate MIPTs in qudit systems using a random quantum circuit model composed of two-qudit Clifford gates. This choice of gate set enables efficient classical simulation without hindering the entanglement dynamics. Our primary goal is to understand how entanglement scaling transitions generalize with increasing local Hilbert space dimension and to characterize the critical behavior and universality of MIPTs in the qudit regime. The thesis is structured as follows:

- **Chapter 2** introduces entanglement in quantum many-body systems, including the different scaling phases and quantitative measures of entanglement. We review entanglement growth and thermalization in one-dimensional random unitary circuits and characterize the measurement-induced phase transition in qubit-based systems.

- **Chapter 3** reviews the theoretical basis for simulating Clifford circuits in higher-dimensional Hilbert spaces. We define the generalized Pauli and Clifford groups, and discuss projective measurements in qudit systems using the stabilizer formalism. Lastly, we reformulate the selected entanglement measures within this framework.

- **Chapter 4** presents the results of our numerical study of MIPTs in qudit random Clifford circuits for $q \geq 2$. We begin with the analysis of unitary dynamics, observing convergent entanglement growth rates. We then introduce measurements to observe the phase transition. We identify the critical measurement rates for varying q and examine the universality of the critical scaling.

- **Chapter 5** extends our investigation to the large-q limit. We construct a classical dynamical model based on stabilizer dynamics, to analyze the entanglement structure present in one-dimensional lattices.

- **Chapter 6** summarizes the key findings of the thesis and outlines directions for future research, including designing measurement protocols in the classical limit, characterization using multipartite entanglement measures, and exploring topological order in monitored qudit circuits.

Chapter 2

Entanglement transitions in random quantum circuits

We begin by reviewing the relevant literature on entanglement phase transitions in random quantum circuits. Herein, we start by introducing the notion of entanglement in quantum many-body systems and outline standard measures for its quantification. This includes a discussion of entanglement scaling, and distinguishing between extensive and sub-extensive regimes. We then turn to the random unitary circuit model on one-dimensional lattices. Using a qubit lattice as an instructive tool, we study entanglement growth and thermalization in isolated quantum systems. Subsequently, we explore how the dynamics of entanglement are altered in the presence of local measurements, leading to the emergence of measurement-induced entanglement transitions. Finally, we examine various quantities employed in the characterization of these transitions, as well as discuss the viability of observing the entanglement transitions on current experimental platforms.

2.1 Entanglement in quantum many-body systems

In quantum information science, entanglement plays the native role of a resource in various protocols, such as state preparation via entanglement swapping [11], measurement-based quantum computation [62], and cryptography protocols such as quantum data-hiding [63]. In the context of quantum many-body systems, entanglement serves as a basis for characterizing correlations between subsystems. While measures of entanglement often omit a system's microscopic details, they instead identify novel phases [64], topological ordering [19], or determine universal properties describing quantum critical points [18]. The understanding of entanglement structures has also been instrumental in the development of efficient tensor network protocols such as the density matrix renormalization group (DMRG) [22]. In this work, we focus on one-dimensional many-body quantum systems defined on periodic lattices. Such a system consisting of L particles can be described by a pure-state wavefunction $|\psi\rangle$, which lies in the composite Hilbert space, defined as

$$\mathcal{H} = \mathcal{H}_1 \otimes \mathcal{H}_2 \otimes \cdots \otimes \mathcal{H}_L, \tag{2.1}$$

where each individual Hilbert space $\mathcal{H}_i$ is a q-dimensional finite vector space ($\mathbb{C}_\mathfrak{q}$), which satisfies the inner product $\langle\phi|\psi\rangle = \sum_{j=1}^{q} \overline{\phi_j} \cdot \psi_j$. The Hilbert space inner product is linear in the second argument, positive ($\langle\phi|\phi\rangle \geq 0 \forall |\psi \neq 0\rangle$), and symmetric under conjugation ($\overline{\langle\phi|\psi\rangle} = \langle\psi|\phi\rangle$).

The composite Hilbert space of a quantum system grows exponentially with system size, scaling as $\dim(\mathcal{H}) = q^L$. This exponential scaling is usually prohibitive for numerical analyses of both equilibrium properties and non-equilibrium dynamics. However, in many physically-motivated settings, this scaling can be mitigated. For example, the presence of local conser-

vation laws enables block diagonalization of the Hamiltonian, effectively reducing the computational complexity. Similarly, when quantum states exhibit low entanglement, efficient tensor network representations can be employed to simulate large systems with high accuracy.

A generic pure state sampled from the *L*-partite description of the Hilbert space in Eq. (2.1) can be represented as

$$|\psi\rangle = \sum_{\{\alpha_i\}=1}^{q} c_{\alpha_1,\alpha_2\cdots\alpha_N} \ |\alpha_1\rangle \otimes |\alpha_2\rangle \otimes \cdots \otimes |\alpha_N\rangle, \qquad (2.2)$$

where the overlap coefficients satisfy $\sum_{\{\alpha_i\}=1}^{q} |c_{\alpha_1,\alpha_2\cdots\alpha_N}|^2 = 1$, and the summation accounts for every tensor product combination of the q-dimensional local basis state $|\alpha_i\rangle$.

To gain a firmer analytical handle on this general representation, we divide the composite Hilbert space into two complementary contiguous segments, $\mathcal{H} = \mathcal{H}_A \otimes \mathcal{H}_B$, i.e., by performing a *bipartition*, with local Hilbert space dimensions q_A and q_B. We can assume that $q_A \leq q_B$ without a loss of generality. On a one-dimensional periodic lattice, the bipartition can be represented by the Fig. 2.1a. The pure state wavefunction now reads:

$$|\psi\rangle = \sum_{\alpha_A=1}^{q_A} \sum_{\alpha_B=1}^{q_B} c_{\alpha_A,\alpha_B} \ |\alpha_A\rangle \otimes |\alpha_B\rangle. \qquad (2.3)$$

In order to quantify the correlations across the bipartition, we perform a singular value decomposition (SVD) to diagonalize the coefficient matrix c_{α_A,α_B}. We obtain $c_{\alpha_A,\alpha_B} = U\Lambda_{AB}V$, where U and V are isometries connecting the two Hilbert spaces $\mathcal{H}_\mathcal{A}$ and $\mathcal{H}_\mathcal{B}$, respectively. The diagonal matrix $\Lambda_{AB} = \sum_{j}^{\min(q_A,q_B)} \lambda_j |j\rangle\langle j|$ is positive semidefinite, composed of the singular values λ_j. The singular values are the Schmidt coefficients of the biparition, and the number of nonzero Schmidt coefficients is denoted the Schmidt rank. The Schmidt coefficients are the basis for quantifying entanglement, as discussed ahead. Following this decomposition, the wavefunction takes the form

$$|\psi\rangle = \sum_{j} \lambda_j \ |j\rangle_A \otimes |j\rangle_B. \qquad (2.4)$$

The Schmidt decomposition can be performed for any general bipartition, represented by Eq. (2.3). For a normalized wavefunction, the Schmidt coefficients satisfy $\sum_{j=1}^{q} \lambda_j^2 = 1$. In accordance with this normalization, $\{\lambda_j^2\}_{\min(q_A,q_B)}$ are the eigenvalues of the reduced density matrices $\rho_{A(B)} = \text{Tr}_{B(A)} [\rho]$. The shared eigenvalues between the reduced density matrices of a bipartition indicate that the two subspaces share correlations equally. Schmidt coefficients also play a key role in determining whether a transformation between two bipartite states, via deterministic local operations and classical communication (LOCC), is possible, i.e. whether $\exists\, \Lambda_{LOCC} : \Lambda_{LOCC}(|\psi\rangle) = |\phi\rangle$. This is ascertained by comparing the partial orderings of the states' respective Schmidt coefficients [11].

The Schmidt coefficients provide the basis for defining measures of entanglement. A measure of entanglement is any function that is monotonic under LOCC transformations [65]. Given an LOCC transformation $\Lambda_{LOCC} : \mathcal{H} \to \mathcal{H}$, an entanglement measure $E(\rho)$ satisfies the inequality

$$E(\Lambda_{LOCC}(\rho)) \leq E(\rho). \qquad (2.5)$$

Entanglement measures satisfying this inequality are invariant under local unitary transformations, a reversible subset of LOCC operations [11]. The most widely employed measure of entanglement is the von Neumann entropy, defined as:

$$S_{vN}(A) = - \text{Tr}\left[\rho_A \log(\rho_A)\right] = - \sum_j \lambda_j^2 \log\left(\lambda_j^2\right). \tag{2.6}$$

Operationally, the von Neumann entropy provides an upper bound on the number of maximally entangled bipartite states which can be distilled from a given density matrix ρ [11]. As maximally entangled states are a resource in quantum teleportation, the von Neumann entropy effectively quantifies the number of copies of the state ρ required for performing the teleporation of a quantum state, thereby making it operationally analogous to the classical Shannon entropy, $H(X) = \sum_{x \in X} p_x \log(p_x)$; $\sum_{x \in X} p_x = 1$. When all the Schmidt coefficients of the bipartition are equal to $\frac{1}{\sqrt{q}}$, the state is maximally entangled and the von Neumann entropy is $\log(\min(q_A, q_B))$. For a product state, the Schmidt rank is one, and consequently $S_{vN} = 0$.

A single-parameter generalization of the von Neumann entropy is the Rényi entropy, defined as:

$$S^{(n)}(A) = \frac{1}{1-n} \ \log_q(\text{Tr}[\rho_A^n]). \tag{2.7}$$

In the limit $n \to 1$, the Rényi entropy returns the von Neumann entropy, while in the limit $n \to 0$, it returns the Hartley entropy, $S^{(0)}(A) = \log(\text{rank}(\rho))$. Rényi entropies also lend themselves to experimental measurement [66–68], and are well-suited for numerical simulations too [69].

Another important entanglement measure is the *mutual information*, which captures correlations between two distinct regions of the lattice. It is defined for two subsystems A and B as

$$I(A : B) = S(A) + S(B) - S(A \cup B), \tag{2.8}$$

where the entropy S_A (S_B) can represent an entanglement measure of one's choice. This expression closely resembles the traditional connected correlation function, and serves as an information-theoretic analogue for identifying phases characterized by entanglement [28, 70–72]. The structure and properties of entanglement measures for bipartite systems are well understood [11], and appropriate measures can be selected or constructed to suit one's application.

In this work, Clifford unitaries are the central facet of the circuit dynamics under study. Accordingly, we use the Rényi entropy as our primary entanglement measure, due to its computational tractability in quantum states prepared solely using Clifford operations. We provide a detailed account of this computation in Section 3.5.

2.1.1 Extensive and sub-extensive entanglement growth

The bipartite Schmidt coefficients, and consequently the bipartite entanglement measures of a many-body quantum state, are essential tools for state characterization. A generic quantum many-body Hamiltonian is typically composed of short-range interactions between local degrees of freedom. As a consequence of the collective nature of these interactions, a majority
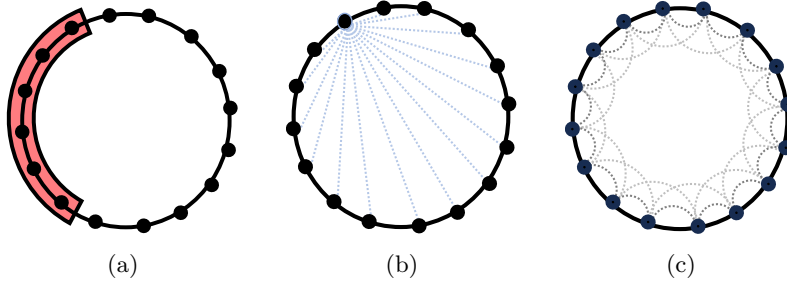
Figure 2.1: (a) Illustration of an arbitrary bipartition on a one-dimensional periodic lattice. (b) Example of extensive entanglement scaling, with significant correlations between individual qubits and the entire lattice. (c) Example of sub-extensive entanglement scaling, showing correlations limited to nearest and next-nearest neighbors.

of the eigenstates in the Hamiltonian's spectrum exhibit a thermal behaviour, with an extensive growth in the thermal entanglement entropy across a bipartition, i.e., $S(A) \propto O(|A|^d)$, where $d = 1$ is the geometric dimension of our lattice. More precisely, the thermal entropy across the bipartition attains an average value given by $S_{\text{page}} \propto |A| \log_q(q_A) + O(1)$, where $|A|$ and q_A denote the volume and the Hilbert space dimension of the bipartition respectively. The growth of the thermal entanglement entropy proportional to the bipartition's size is referred to as *volume-law* scaling. An intuitive illustration of the volume-law is shown in Fig. 2.1b. Therein, non-negligible correlations, represented by dotted lines, are shared between each degree of freedom on the one-dimensional periodic lattice.

An opposing configuration, shown in Fig. 2.1c, is obtained when degrees of freedom interact locally, or in general, are not maximally correlated. In this situation, measures of entanglement scale sub-extensively ($S(A) \propto O(|A|^{d-1})$), proportional to the boundary area of the biparition, thereby denoting this as the *area-law* regime. A sparse number of states exhibit such a non-thermal entanglement scaling in the spectrum of a quantum many-body Hamiltonian. Some salient examples of states fulfilling the an area-law scaling include: ground states of gapped local-Hamiltonians which lie in the subspace composed of states with low Schmidt ranks [73], many-body localized eigenstates where the local integrals of motion prohibit thermalization and extensive entanglement growth [74], and topologically ordered ground states where long-range correlations exist in the absence of eigenstate thermalization [19, 64].

2.2 Entanglement growth in random unitary circuits

We now utilize the quantum entanglement measures to study entanglement growth under unstructured, random unitary evolution. Particularly, we consider entanglement growth in a one-dimensional, periodic system composed of q-level particles. The evolution proceeds in discrete time steps, in a layered brickwork-like pattern, depicted in Fig 2.2. This discrete evolution of the quantum state is denoted the *quantum circuit* representation. While this *quantum circuit* resembles the evolution of a system in the time-evolving block decimation (TEBD) algorithm [24, 75], the brickwork structure of the TEBD evolution is dependent upon the matrix norm between the unitaries and the identity matrix being vanishingly small. However, this constraint does not apply here. Instead, we restrict the unitaries to be randomly drawn elements of the 2-qudit Clifford group $\text{Cl}(q, 2)$. Sampling unitaries from the Clifford group provides a good approximation to unitaries sampled uniformly without constraints, as

the Clifford group is a unitary 2-design on the Haar measure. Furthermore, Clifford circuits permit efficient large-scale classical simulations, up to a 1000 qubits. The properties of the Clifford group are discussed further in Chapter 3, with sampling techniques outlined in Appendix B.
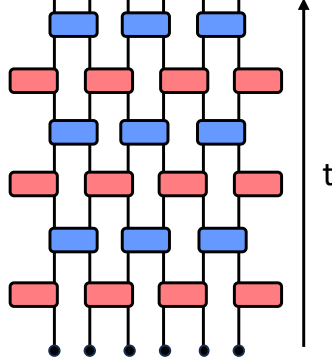
Figure 2.2: Schematic of a 1D random unitary circuit composed of 2-qubit gates arranged in a brickwork structure.

Entanglement growth under random unitary dynamics, also referred to as *noisy* entanglement growth, has been well-studied in one-dimensional lattice models. In particular, the results of Ref. [76] show that entanglement growth under random unitary dynamics conforms to the Kardar-Parisi-Zhang (KPZ) universality class. The KPZ universality class follows from the nonlinear Langevin equation [77],

$$\frac{\partial h(\overline{x}, t)}{\partial t} = \nu \, \nabla^2 h(\overline{x}, t) + \frac{\lambda}{2} (\nabla h(\overline{x}, t))^2 + \eta(\overline{x}, t). \tag{2.9}$$

This equation describes a broad range of stochastic surface growth phenomena. Here $h(\overline{x}, t)$ represents the height of the surface, and the parameters ν and λ account for the dependence of the surface growth on the surface tension and its gradient respectively. The stochastic component $\eta(\overline{x}, t)$ adds gaussian noise, which satisfies $\langle \eta(\overline{x}, t) \rangle = 0$. The fluctuations in the surface height scale with the exponent $\beta = \frac{1}{3}$, one of the key characteristics of this universality class. A direct analogy can be drawn between the stochastic surface growth modelled by Eq. (2.9), and the growth of bipartite entanglement entropies in a one-dimensional lattice, leading to the average bipartite entropy to be described as [76]

$$\langle S(\overline{x}, t) \rangle = v_E t + B t^\beta. \tag{2.10}$$

The slope of the linear growth v_E and the coefficient of the fluctuations B, are not universal under KPZ dynamics. As the unitaries in the brickwork circuit are randomly selected, the thermal pure state conforms to volume-law scaling of biparite entanglement entropies. Hence, the slope v_E can be interpreted as the speed governing the spread of entanglement, or thermalization, in the one-dimensional lattice. In Ref. [76], it is shown that v_E is slower than the *butterfly velocity* v_B, which governs the spreading of operator supports, implying that operator growth precedes thermalization. The thermal value of the entropy $S(\overline{x})$ is attained in a polynomial number of steps $O(L)$ [78].

In finite-dimensional local Hilbert spaces, the analogy between the stochastic surface growth model and the noisy entanglement growth can be formalized for the Hartley entropy,

$S_0(x)$, as

$$S(x, t+1) = \min \left[S(x-1, t), S(x+1, t) \right] + 1. \tag{2.11}$$

However, Rényi entropies converge in the limit of large local Hilbert space dimensions ($q \gg 1$) [76], and thereby, satisfy Eq. (2.11) in this limit.

2.3 Measurement-induced entanglement transitions

While entanglement measures tend to thermalize rapidly under random unitary evolution, their steady-state values are affected by the presence of local measurements and peturbations. These local measurements introduce a competing mechanism to the unitary dynamics: while the two-qudit Clifford unitaries locally raise entanglement, projective measurements can reduce it in a non-local manner. The interplay between these *entangling* and *disentangling* processes is the central focus of this study.

In this section, we introduce the *measurement-induced entanglement transition* in the simplest setting of ($q = 2$), as a precursor to the general results for $q > 2$ presented in Chapter 4. We begin by incorporating the random unitary circuit with single-qubit projective measurements in the computational basis. A single time step in the simulation consists of two layers of two-qubit Clifford unitaries, as illustrated in Fig. 2.3. The first layer acts on all odd-indexed qubit pairs, followed by a second layer acting on even-indexed pairs. After each layer, single-qubit measurements are applied with probability p to each qubit. To eliminate artifacts introduced by the underlying brickwork structure, we compute and average entanglement entropies following each unitary layer.
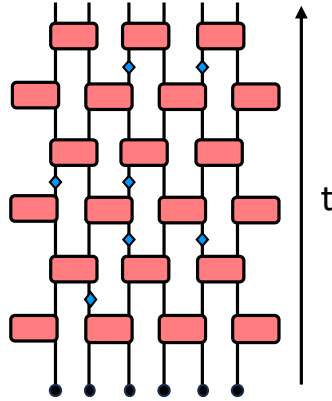

Figure 2.3: Schematic of the 1D random quantum circuit used to study the measurement-induced entanglement transition. The circuit consists of two-qubit unitaries arranged in a brickwork pattern, with probabilistic local projective measurements shown in blue.

Using this setup, we first examine the growth and thermalization of the entanglement entropy, shown in Fig. 2.4. In the absence of measurements, the unitary circuit reaches a thermal entanglement entropy $S_A \approx L/2$, in agreement with predictions of the surface growth analogy of Ref. [76]. However, with a linear increase of the measurement rate, the steady-state value of the entanglement entropy is suppressed. For sufficiently high measurement rates, no effective entanglement growth occurs and the system is confined to a product state in the computational basis, thereby exhibiting a quantum Zeno effect [79]. Although the initial state used in Fig. 2.4 is the vacuum state $|0\rangle^{\otimes L}$, the thermal entanglement entropies

depend only upon the rate of measurement interspersed within the random unitary circuit, and not on the specific choice of initial state [29]. Prior to thermalization ($t < T_{therm}$), the bipartite entanglement entropy, in the thermodynamic limit, scales as

$$S_A(t, L \to \infty) \propto \begin{cases} t & p < p_c \\ \log(t) & p = p_c \, , \\ \text{constant} & p > p_c \end{cases} \qquad (2.12)$$

where the critical measurement rate p_c and the corresponding color gradient in Fig. 2.4, hint at the central phenomenon of interest: the transition in entanglement scaling.
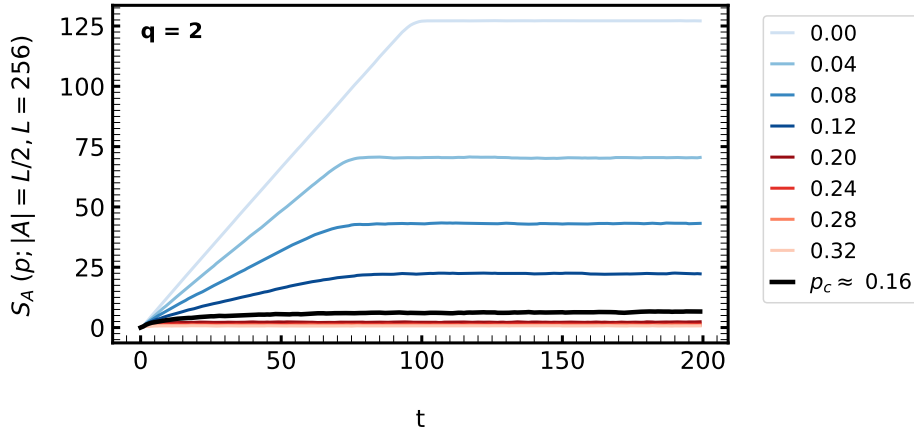
Figure 2.4: Entanglement entropy S_A as a function of time for different measurement rates in a $q = 2$ random Clifford circuit. Without measurements, entropy saturates to a thermal value $S_A \approx L/2$, while increasing measurement rates suppresses the saturation value. The entropy follows the scaling described in Eq. (2.12) prior to $T_{therm} \approx 100$.

To observe the phase transition explicitly, we examine the thermal bipartite entanglement entropy as a function of the system size. As shown in Fig. 2.5, a clear difference in scaling emerges across measurement regimes. For low measurement rates, the entropy grows linearly with the system size, indicative of volume-law behavior in one-dimension. For higher measurement rates, the entropy is independent of the system size, consistent with an area law behaviour. Between these regimes lies a critical measurement rate p_c exhibiting a logarithmic scaling with the system size, marking a continuous entanglement scaling transition, akin to a second-order phase transition. The scaling of thermal bipartite entanglement entropies can be summarized as

$$S_A(t \to \infty, L) \propto \begin{cases} |A| & p < p_c \\ \log(|A|) & p = p_c \, , \\ \text{constant} & p > p_c \end{cases} \qquad (2.13)$$

A further analysis of these scaling forms in Eq. (2.12) and Eq. (2.13) can be found in Ref. [29].

While Fig. 2.5 offers an instructive visualization of the entanglement scaling transition, identifying the location of the critical measurement rate from entropy scaling alone can be imprecise. To identify the transition more accurately, we consider two additional quantities: the rescaled thermal entanglement entropy S_A/L and a disjoint mutual information measure. These are shown in Fig. 2.6. The rescaled entropy S_A/L serves as an order parameter,

capturing the transition from volume-law scaling where $S_A/L > 0$, to area-law scaling where $S_A/L = 0$.

For the disjoint mutual information, we select two regions, denoted A and B, each of length $L/8$, with their centers separated by a distance $L/2$ on the one-dimensional periodic lattice. This quantity, defined in Eq. (2.8), captures the correlations shared exclusively between these two regions. Away from the critical point, the mutual information is exponentially suppressed [29]. For high measurement rates, the system is effectively disentangled, implying $S_{A \cup B} \approx S_A + S_B$. As only short-range correlations remain, we find that the mutual information vanishes. For low measurement rates, although long-range entanglement exists, correlations are delocalized throughout the system, and not constrained exclusively to the regions A and B. This, again, results, in suppressed mutual information. Near the critical measurement probability p_c, the existence of exclusive correlations between the subsystems A and B is reflected through a sharp peak. The height of the peak is convergent under increasing system size, reflecting an emergent conformal field theory description at the critical point [29]. The critical exponent of the correlation length can be extracted using the finite-size scaling forms for the thermal entanglement entropy (Fig. 2.5) and the mutual information (Fig. 2.6a).
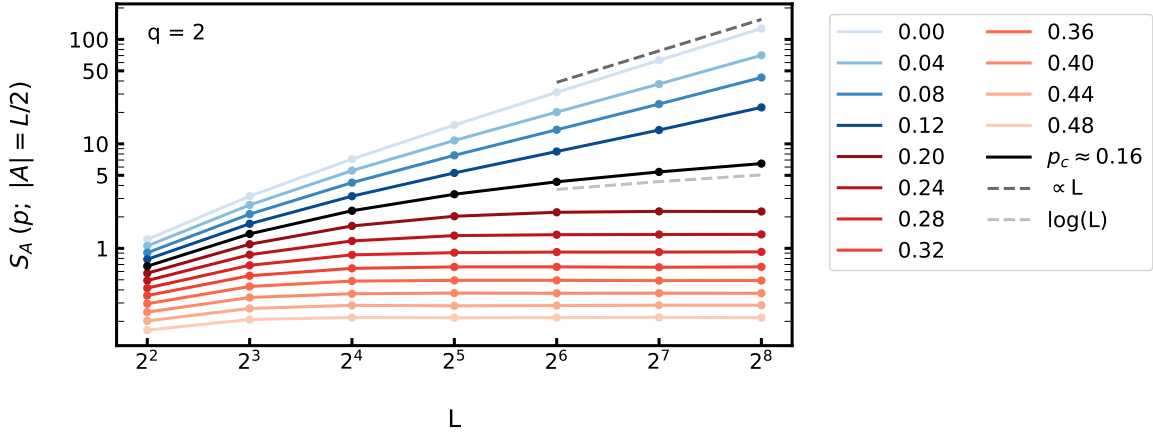

Figure 2.5: Thermal entanglement entropy as a function of the system size for various measurement rates in a $q = 2$ Clifford circuit. The scaling transitions from a volume law (blue) to an area law (red), with logarithmic scaling at the critical measurement rate p_c, indicating a continuous measurement-induced phase transition.

2.3.1 Challenges in experimental realization

So far, we've considered a simple model that exhibits a measurement-induced entanglement transition. This model was comprised of merely two components, two-qubit unitary gates and local projective measurements. These minimal requirements are also shared by other measurement-induced phase transitions, such as the *purification transition*, wherein local measurements drive a mixed-state density matrix towards a pure state. These two components, are typically easily accessible on modern quantum simulation or computing platforms. However, despite the apparent simplicity of the setup, the experimental realization of measurement-induced phase transitions poses a significant challenge, known as the *post-selection problem*.

At the first glance, single-qubit measurements may resemble local perturbations occurring

(a)

(b)
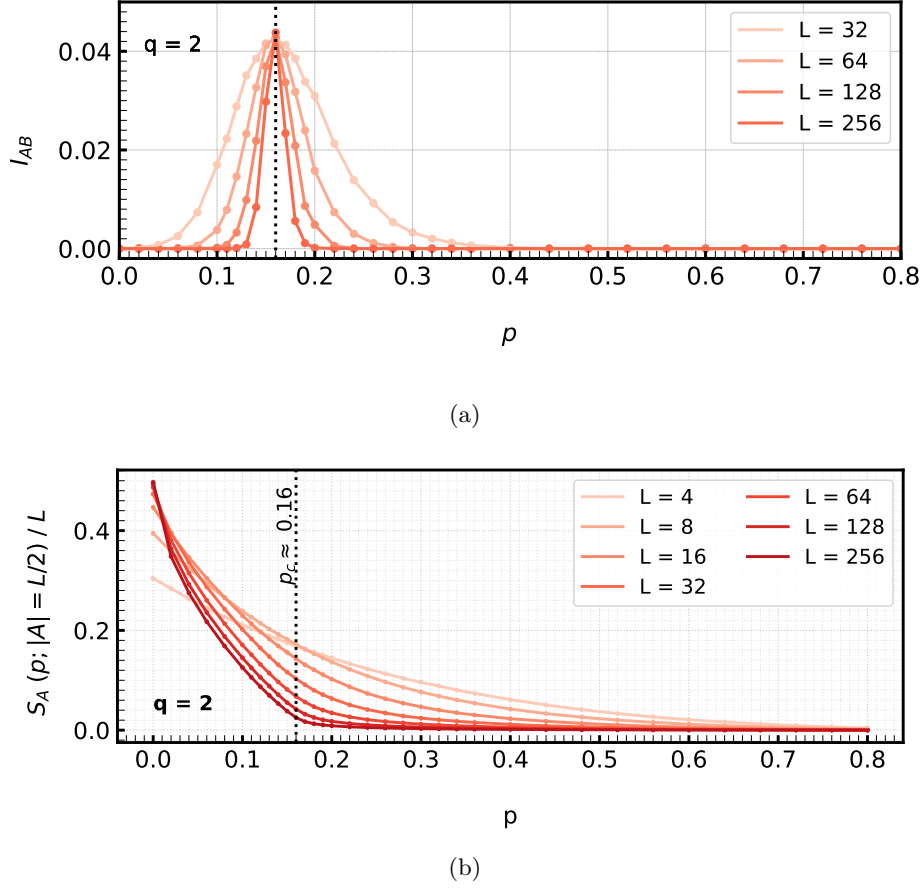
Figure 2.6: Measures of precisely identifying the measurement-induced entanglement transition in a $q = 2$ random Clifford circuit. (a) Disjoint mutual information between two diametrically opposite regions of size $L/8$. The sharp peak indicates the critical measurement rate p_c. (b) Rescaled entropy S_A/L as an order parameter for the MIPT. In the thermodynamic limit, it remains finite in the volume-law phase and vanishes in the area-law phase.

due to noisy environmental processes around the system. Such local perturbations also act locally and disturb a qubit's state. However, the post-measurement state is distinct from the post-perturbation state. After a measurement, the recording of the outcome enables the post-measurement state to be described by a pure state density matrix, conditioned on the outcome. Whereas, the action of arbitrary local perturbations is not known, and hence, the post-perturbation state is described as a mixed state density matrix, represented as a weighted ensemble of pure states. This latter process is simply *decoherence.*

This difference can be illustrated in the following manner. Consider a quantum subsystem coupled to a bath which can interact with individual degrees of freedom of the quantum subsystem. We now follow a similar protocol, as employed for measurement-induced phase transitions, i.e., we permit the quantum subsystem to attain a thermal state with respect to its bipartite entanglement entropies, for varying subsystem-bath coupling strengths. As the rate of perturbation increases, every subsequent local perturbation will decohere the quantum subsystem further. The mixed state density matrix will then converge towards the maximally mixed state, i.e., the normalized identity matrix. Such a maximally mixed thermal state cannot exhibit a critical behaviour for varying coupling strengths. Thus, to observe the critical behaviour, one must keep track of the measurement outcomes, and the quantum subsystem must be projected into the corresponding pure state after each measure-

ment. This process referred to as *post-selection.*

Although tracking measurement outcomes is straightforward, the challenge arises due to the inherent randomness in the outcome of quantum mechanical measurement. For a randomly generated circuit configuration and its corresponding sequence of measurement outcomes, the required steady pure state can only be obtained when an experimental run yields the desired sequence of outcomes. For a q-dimensional qudit, each of the q outcomes is equally likely. Hence, to obtain a successful experimental run, the post-selection protocol demands that a large number of identical initial state be prepared. Specifically, for a circuit comprising of m measurements, one would require $O(q^m)$ identical initial states to be prepared. Furthermore, as the measurements are performed at each qudit, the number of measurements satisfies $m \propto L \cdot T \cdot p$, where T is the number of timesteps and p is the rate of measurement. This prerequisite of initial state preparation makes a substantially large experimental realization resource intensive.

Despite the bottlenecks imposed by post-selection and the decoherence in experimental hardware, several promising protocols and experimental realizations have emerged. One salient protocol bypasses post-selection using space-time dualities. Herein, a mapping from the hybrid circuits with mid-circuit measurements to dual circuits composed solely of unitary gates is identified [80]. This protocol has shown experimental promise [81], however, the duality mapping is viable for a limited set of circuit compositions, and does not extend to circuits composed Haar-random unitaries. Some experimental strategies address post-selection more directly. For example, Ref. [82] performs the aforementioned resource-intensive post-selection, while Ref. [83] employs dynamic feedback loops to circumvent post-selection altogether. While these protocols have yielded successful experimental observations of measurement-induced phase transitions, the inherent resource requirements are a significant constrain on the system size. On the theoretical front, two more classes of protocols have gained recognition. One entails the entangling of an ancillary qubit to the system. Then, the time required to disentangle the ancilla, employing classical decoders, serves as the marker for the entanglement phase of the system [84]. The other class of protocols employ *cross-measures*, i.e. correlations between an experimental run and a classical simulation, as order parameters for the entanglement transition [85–87]. The use of classical simulations and decoders, however, is facilitated using Clifford-only unitary circuits, thereby restricting the protocols from involving Haar-random unitaries again. However, in a recent work, tree-tensor network representations of the quantum state have shown potential for efficient classical decoding beyond the Clifford-unitary circuit [88], exploiting the recursive structure of the representation.

Chapter 3

Theory of Clifford circuit simulation

In this chapter, we will review the theory supporting the simulation of random Clifford circuits, which are utilized in the following study of measurement-induced entanglement scaling transitions. We utilize the Clifford group, a central and versatile tool in quantum information theory and quantum computing, which extends Gottesman's formulation of stabilizer states [89] from the context of quantum error correction to gate-based simulations of a broader class of protocols [90]. Crucially, quantum protocols which can be expressed purely in terms of Clifford group operations can be efficiently simulated on a classical device.

This capacity for efficient classical simulation has driven extensive studies of into the rich structure of the Clifford group, yielding multiple efficient representations and simulation methodologies. These include the stabilizer tableau representation and its variants [91], the graph state representation [92], and the so-called affine form of Cliffords [93]. Each representation grants different analytical handles suited to unique applications. For instance, the traditional stabilizer tableau provides an efficient means of analysing quantum error correction protocols [94], while the graph state representations grants a lens to view entanglement as a resource, paving the way for measurement-based quantum computing [95, 96]. Efficient Clifford simulations can also entail efficient sampling of its elements, discussed further in Appendix B.

One notable application of the Clifford group is in the characterization and verification of quantum protocols, and near-term intermediate-scale quantum (NISQ) hardware, through randomized benchmarking (RB) [97, 98]. In a traditional RB protocol, the target gates are interleaved with randomly-sampled Clifford gates, to characterize average channel noise and fidelity. Moreover, the L-qudit Clifford group forms a unitary 2-design [99], an algebraic structure that facilitates the development of efficient randomized benchmarking protocols using its elements [100].

Beyond efficient simulation and characterization, the Clifford group plays a key role in the construction of universal gate sets for quantum computation. Inclusion of any non-Clifford gate, typically the single-qubit T-gate ($\pi/8$ gate), to the Clifford group yields the universal gate set [101]. The inclusion of such non-Clifford operations significantly increases the complexity of classical simulation. The number of non-Clifford, alternatively non-stabilizer, resources required to perform a quantum operation are often referred to as 'magic'. The quantification of magic is an area of inquiry for the optimization of classical simulations of quantum protocols [102–104].

As contemporary quantum simulators and NISQ hardware utilize qubits, much of the experimental and computational work focuses on the qubit Clifford group. However, the algebraic structure and classical simulability of the Clifford group extends naturally to higher local Hilbert space dimensions [99], prompting the extension of randomized benchmarking

to higher-dimensional local Hilbert spaces as well [105, 106]. We begin our discussion by defining the generalized Pauli and Clifford groups for q-dimensional systems, which describe qudit states and their transformations, respectively. They constitute key components of the subsequently detailed stabilizer representation in higher-dimensional local Hilbert spaces. In these discussions, we often utilize the case $q = 2$ as a didactic example, before presenting a general framework for the simulation of random quantum circuits for prime-dimensional q. Finally, we review the incorporation of local projective measurements into the stabilizer formalism, and reformulate the Rényi entropies within this setting.

While the formulations of the Pauli group and Clifford group detailed below are valid in arbitrary local Hilbert space dimensions [99, 107], operating within prime-dimensional local Hilbert spaces provides certain structural advantages. Specifically, the finite-field $\mathbb{F}_q$, with q elements, provides a cyclic arithmetic structure with multiplicative inverses defined for each element. This simplifies protocols involving the modulation of commutation relations and facilitates an efficient measurement protocol.

3.1 Generalized Pauli group

In the stabilizer formalism, we consider Clifford circuits through their action on Pauli operators, rather than representing Clifford elements as explicit matrices. This representation is central to efficient simulation in the stabilizer formalism. Hence, Pauli operators provide a natural basis for representing both quantum states and unitary operations. In the single-qubit case ($q = 2$), the Pauli group consists of the matrices $\{X, Y, Z, \mathbb{I}\}$, defined as:

$$X = \begin{pmatrix} 0 & 1 \\ 1 & 0 \end{pmatrix}, \quad Y = \begin{pmatrix} 0 & -i \\ i & 0 \end{pmatrix}, \quad Z = \begin{pmatrix} 1 & 0 \\ 0 & -1 \end{pmatrix}, \quad \mathbb{I} = \begin{pmatrix} 1 & 0 \\ 0 & 1 \end{pmatrix}. \tag{3.1}$$

The group is closed under matrix multiplication upon the inclusion of global phases $\{\pm 1, \pm i\}$. This inclusion yields a finite group consisting of 8 elements, which are generated by $\langle X, Z \rangle$.

Generalizations of the Pauli group to higher local Hilbert space dimension cannot retain the simple Hermitian unitary matrices presented in the qubit case Eq. (3.1). There are two prominent generalizations of the qubit Pauli group: the Gell-Mann matrices, which preserve the Hermiticity of the operators [108], and the Weyl-Heisenberg (WH) matrices, which preserve their unitarity [109, 110]. While both the Gell-Mann and Weyl-Heisenberg matrices represent the Pauli group as q-dimensional square matrices over the finite field $\mathbb{F}_q$, the WH matrices also support the stabilizer representation for qudit systems, and are thus adopted in this work.

The Weyl-Heisenberg generalization of the Pauli group is composed of the clock operator ($Z_{\mathfrak{q}}$) and the shift ($X_{\mathfrak{q}}$) operator, defined by the following actions on the computational basis states $\{|j\rangle\}_{j=0}^{q-1}$:

$$\begin{aligned} Z_{\mathfrak{q}} |j\rangle &= \omega^j |j\rangle, \\ X_{\mathfrak{q}} |j\rangle &= |j+1 \bmod q\rangle, \end{aligned} \tag{3.2}$$

where $\omega = e^{2\pi i/q}$ is a primitive q-th root of unity [44]. The exponents of the WH matrices are q-periodic under self-exponentiation, i.e.,

$$X_{\mathfrak{q}}^q = Z_{\mathfrak{q}}^q = \mathbb{I}. \tag{3.3}$$

In the computational basis, the clock-operator (Z_{q}) is a diagonal matrix composed of the roots of unity, and the shift-operator (X_{q}) forms an q-cyclic permutation matrix. As an illustrative example, for $q = 3$ the WH operators are:

$$X_3 = \begin{pmatrix} 0 & 0 & 1 \\ 1 & 0 & 0 \\ 0 & 1 & 0 \end{pmatrix}, \qquad Z_3 = \begin{pmatrix} 1 & 0 & 0 \\ 0 & \omega & 0 \\ 0 & 0 & \omega^2 \end{pmatrix}. \tag{3.4}$$

Analogous to the qubit case, the single-qudit Pauli group is generated by the Weyl-Heisenberg operators, $\mathcal{P}(q, 1) = \langle X_{\mathsf{q}}, Z_{\mathsf{q}} \rangle$, and is closed under multiplication upon inclusion of the q-th roots of unity $\{\omega^j\}$ as global phases, where $j \in \{0, \ldots, q-1\}$. A general single-qudit operator then takes the form

$$\omega^\alpha X_{\mathsf{q}}^r Z_{\mathsf{q}}^s, \quad \text{for } \alpha, r, s \in \mathbb{Z}_q, \tag{3.5}$$

and satisfies the commutation relation:

$$(X_{\mathsf{q}}^r Z_{\mathsf{q}}^s)(X_{\mathsf{q}}^t Z_{\mathsf{q}}^u) = \omega^{st-ru}(X_{\mathsf{q}}^t Z_{\mathsf{q}}^u)(X_{\mathsf{q}}^r Z_{\mathsf{q}}^s). \tag{3.6}$$

To simulate one-dimensional L-qudit systems, we extend this construction to the L-qudit Pauli group $\mathcal{P}(q, L)$, defined as a string of tensor products of single-qudit WH operators:

$$\mathcal{P}(q, L) = \left\{ \omega^\alpha \bigotimes_{i=1}^{L} X_{\mathsf{q}}^{r_i} Z_{\mathsf{q}}^{s_i} \ \middle| \ \alpha, r_i, s_i \in \mathbb{Z}_q \right\}. \tag{3.7}$$

Following the single-qudit case, the group $\mathcal{P}(q, L)$ is finite and closed under multiplication, with cardinality q^{2L+1}. Each string of unitary operators of this group can be compactly represented classically. In particular, a Pauli string with global phase requires at most $(2L + 1) \cdot \lceil \log_2 q \rceil$ bits to store. Here, $\lceil \log_2 q \rceil$ bits are required to store an integer modulo-q, the $2L$ terms track the exponents of X_{q} and Z_{q} at each site, and the final term accounts for the global phase.

3.2 Generalized Clifford group

The L-qudit Clifford group $\mathrm{Cl}(q, L)$ is employed here for performing state evolution in stabilizer formalism. It is defined as the group of unitary operators over the q^L-dimensional Hilbert space that map elements of the generalized Pauli group to other Pauli operators under conjugation:

$$\mathrm{Cl}(q, L) = \{ V \in \mathrm{U}(q^L) \mid V\mathcal{P}V^\dagger = \mathcal{P} \}, \tag{3.8}$$

where $\mathcal{P}(q, L)$ is the L-qudit Pauli group. Thus, the Clifford group forms the *normalizer* of $\mathcal{P}(q, L)$. As the normalizing action of the Clifford group proceeds via unitary conjugation, it is unique up to a global phase. Further, as unitary conjugation is a linear map, the commutation relations between generalized Pauli operators are invariant under the action of a Clifford unitary,

$$X_{\mathsf{q}} Z_{\mathsf{q}} = \omega^{-1} Z_{\mathsf{q}} X_{\mathsf{q}} \xrightarrow{U} U X_{\mathsf{q}} Z_{\mathsf{q}} U^\dagger = \omega^{-1} U Z_{\mathsf{q}} X_{\mathsf{q}} U^\dagger, \quad \forall U \in \mathrm{Cl}(q, L). \tag{3.9}$$

Since the global phase $e^{i\theta}\mathbb{I}$ also satisfies Eq. (3.8), the Clifford group contains infinitely many elements. Hence, in the context of Clifford circuit simulations, it is more suitable to

work with the the *projective* Clifford group $\overline{\mathrm{Cl}}(q, N) = \mathrm{Cl}(q, N)/\mathrm{U}(1)$. Through this discretization, we exclude the trivial equivalence between elements induced by a global phase on the Clifford transformation. The cardinality of this projective group scales exponentially with number of qudits and their local Hilbert space dimension (see Appendix A).

In the case $q = 2$, the Clifford group can be reduced to three generators: the Hadamard (H), phase (S), and controlled-NOT (CNOT) gates [90, 111]. The actions of these generators can be extended to higher local Hilbert space dimension ($q > 2$) [44, 105, 107].

- The Hadamard gate generalizes to a Fourier gate (F), which creates a phase-weighted superposition of all computational basis states, as:

$$|j\rangle \longrightarrow \sum_{k=0}^{q-1} \omega^{jk} |k\rangle, \tag{3.10}$$

- Generalizations of the phase gate (S) depend on the Hilbert space dimension [105]. In prime-dimensional Hilbert spaces, its action is:

$$|j\rangle \longrightarrow \omega^{j(j-1)/2} |j\rangle, \tag{3.11}$$

- The CNOT gate generalizes to a modular SUM gate on the computational basis:

$$|j\rangle |k\rangle \longrightarrow |j\rangle |(j + k) \mod q\rangle, \tag{3.12}$$

- The controlled-Z (CZ) gate is a standard alternative to the CNOT as a two-qudit Clifford generator, with the action:

$$|j\rangle |k\rangle \longrightarrow \omega^{jk} |j\rangle |k\rangle. \tag{3.13}$$

These generalizations can be reformulated as transformations of L-qudit Pauli operators [44]. For illustration, in the case $q = 3$, the action of the SUM gate on a Pauli string is:

$$\mathbb{I} \otimes Z \otimes X \xrightarrow{\mathrm{SUM}_{12}} Z^2 \otimes Z \otimes X. \tag{3.14}$$

For a quantum circuit protocol relying on a fixed subset of the Clifford group, the necessary Clifford unitaries can be constructed straightforwardly from the aforementioned generators. However, the simulation of random Clifford circuits requires uniform sampling of the elements of $\overline{\mathrm{Cl}}(q, L)$. This task is computationally demanding due to the exponential growth of the projective Clifford group.

Several algorithms have been formulated to tackle this problem [111–114]. For instance, the widely adopted approach of Ref. [111] introduces an algorithm for simulating random qubit Clifford circuits by sequentially applying the generators of the qubit Clifford group. In our work, we extend the method outlined in Ref. [29] to prime q, enabling uniform generation of Clifford elements in higher local Hilbert spaces. Using this approach, one systematically constructs the full set of Clifford group elements, followed by uniform sampling from this set. A detailed discussion of our implementation, alongside alternative efficient sampling strategies, is provided in Appendix B.

We conclude this section by highlighting a crucial property of the Clifford group, i.e., its role as a *unitary 2-design* [99]. This means that the finite Clifford group can exactly

reproduce averages over the Haar measure, for functions which are linear and quadratic in the unitary conjugation [105]. This is formalized as [100, 105]:

$$\frac{1}{\left|\tilde{\mathrm{Cl}}(q,N)\right|} \sum_{j=1}^{\left|\tilde{\mathrm{Cl}}(q,N)\right|} U_j^\dagger \mathcal{E}(U_j \rho U_j^\dagger) U_j = \int_{U(q)} dU \; U^\dagger \mathcal{E}(U \rho U^\dagger) U, \tag{3.15}$$

where $\mathcal{E}$ is a completely positive trace-preserving (CPTP) map. This property underlies the use of Clifford circuits in randomized benchmarking, where the action of Clifford unitaries reduces a CPTP map to the depolarizing channel [98].

3.3 Stabilizer formalism

The stabilizer representation uniquely describes an L-qudit quantum state $|\psi\rangle$, by identifying it as the mutual eigenstate of a finite set of Pauli operator strings, of the group $\mathcal{P}(q,L)$. These operator strings are denoted as the '*stabilizers*' of the quantum state $|\psi\rangle$. This means, $|\psi\rangle$ is invariant under the unitary action of the stabilizer operator strings, which are unique up to the global phase on $|\psi\rangle$. This framework is a cornerstone of quantum error correction protocols [44, 89].

The set of Pauli operator strings that stabilize $|\psi\rangle$ contains q^L mutually commuting elements, forming a subgroup of the generalized Pauli group that is closed under multiplication. Importantly, the stabilizer subgroup cannot contain $-\mathbb{I}$, as it does not leave $|\psi\rangle$ invariant. Similarly, other non-trivial scalar multiples of the identity, i.e., $\pm i\mathbb{I}$ are not valid stabilizers.

Despite the exponential number of stabilizers, the entire subgroup can be completely specified by L linearly independent stabilizers, denoted by the generating set $\mathcal{G} = \langle g_1, g_2, \ldots, g_L \rangle$. For instance, the stabilizer generators for the maximally entangled two-qudit Bell state $|\phi^+\rangle$ are

$$q = 2 : \quad \left|\phi^+\right\rangle = \frac{1}{\sqrt{2}}(|00\rangle + |11\rangle) \quad \longleftrightarrow \langle X \otimes X, Z \otimes Z \rangle, \tag{3.16}$$

$$q > 2 : \quad \left|\phi^+\right\rangle = \frac{1}{\sqrt{q}} \sum_{i=1}^{q} |ii\rangle \quad \longleftrightarrow \left\langle X \otimes X, Z \otimes Z^{-1} \right\rangle, \tag{3.17}$$

Each L-qudit stabilizer generator g_i is a Pauli operator string, in turn described by $2L$ Pauli generators, $\left\langle \{X_{\mathfrak{q},r}, Z_{\mathfrak{q},r}\}_{r=1}^L \right\rangle$. Hence, after accounting for phases on the generators, the state $|\psi\rangle$ in this framework is described by a $L \cdot (2L+1)$-dimensional matrix, known as the *stabilizer tableau*, rather than an vector of basis overlap coefficients of size q^N. This compression enables the efficient classical simulation and storage.

Any state $|\psi\rangle$ on the stabilizer subgroup's manifold can be prepared by the action of Clifford unitaries on the state $|0\rangle^{\otimes L}$. During state preparation or evolution, the action of a Clifford unitary (V) on the state $|\psi\rangle$ can be tracked by the conjugation of the corresponding stabilizer generator g_i.

$$g_i |\psi\rangle = |\psi\rangle, \tag{3.18}$$

$$(V g_i V^\dagger) \, V |\psi\rangle = V |\psi\rangle \quad \forall \, V \in \mathrm{Cl}(q,L), \tag{3.19}$$

Thus, in numerical simulations, unitary evolution is implemented by updating the generating set $\mathcal{G}(t=0)$:

$$|\psi\rangle \longleftrightarrow \;<g_1, g_2, \ldots, g_N>, \tag{3.20}$$

$$V\,|\psi\rangle \longleftrightarrow \;<V g_1 V^\dagger, V g_2 V^\dagger, \ldots, V g_N V^\dagger> \quad \forall\, V \in \mathrm{Cl}(q, L). \tag{3.21}$$

As Clifford unitary maps preserve commutation relations, the generator $\mathcal{G}(t>0)$ describes a valid stabilizer state.

The framework of state representation and unitary evolution using Clifford operations is formalized by the Gottesman-Knill theorem [12, 90]:

Theorem 3.1 (Gottesman Knill Theorem) *A quantum state that is initialized in the computational basis, evolved unitarily with elements of the Clifford group, and measured using operators in the Pauli group can be weakly simulated efficiently in polynomial time on a classical computer.*

However, this framework cannot be universally employed, as only a subset of quantum states are valid stabilizer states. The number of distinct L-qudit stabilizer states is finite and given by $q^L \prod_{i=1}^{L}(q^i + 1)$ [111, 115]. States that do not reside within the stabilizer manifold can be generated by including non-Clifford unitary gates in the quantum circuit. Provided that the number of required non-Clifford resources remains limited, an efficient preparation of these states remains feasible on a classical device [104].

3.4 Projective measurement in the stabilizer formalism

The final component in simulating monitored random Clifford circuits is the implementation of projective measurements within the stabilizer formalism. Consider a stabilizer state described by a generating set $\mathcal{G}$, and a single-qudit Pauli operator to be measured, A. For a q-dimensional Hilbert space, the eigenvalues of A are ω^a, where a is an element of $\mathbb{Z}_q$. In the $q = 2$ case, operators such as X and Z are Hermitian, and can be interpreted as observables. The corresponding projectors, e.g., $|0\rangle\langle 0|$ and $|1\rangle\langle 1|$, can be constructed straightforwardly. However, for $q > 2$, single-qudit Pauli operators are no longer Hermitian. Consequently, the projectors associated with the eigenvalues ω^a take the form [44, 116]:

$$P_a = \frac{1}{q} \sum_{j=0}^{q-1} \omega^{-aj} A^j. \tag{3.22}$$

To implement a measurement of A in the stabilizer formalism, we first test the commutation relations between A and the generators in $\mathcal{G}$. If A commutes with all elements of $\mathcal{G}$, then the measurement leaves the state invariant, because A itself belongs to the stabilizer group $S = \langle \mathcal{G} \rangle$. Here, the meaurement outcome is deterministically $+1$.

However, if A anticommutes with one or more elements of $\mathcal{G}$, the generating set must be transformed so that exactly one generator anticommutes with A. Since the generating set $\mathcal{G}$ in the stabilizer tableau is not unique, this can be achieved by considering linear combinations of generators. For example, if the generators g_1, g_2, g_3 each anticommute with A, then linear combinations such as $\tilde{g}_2 = g_1^\alpha g_2$ and $\tilde{g}_3 = g_1^\beta g_3$ (for $\alpha, \beta \in \mathbb{Z}_q$) can be constructed, which commute with A [12, 44]. This transformation ensures that only a single generator g_1 anticommutes with A.

Particularly, assume that anticommutation satisfies the relation $g_1 A = \omega A g_1$. For prime q, this assumption is always true for some g_1^{γ}, where γ is an element of $\mathbb{Z}_q$. Then, we can compute the probabilities of the measurement outcomes:

$$p(a) = \mathrm{Tr}(P_a \, |\psi\rangle\langle\psi|) \tag{3.23}$$

$$= \mathrm{Tr}\left(P_a g_1 \, |\psi\rangle\langle\psi| \, g_1^{\dagger}\right) \tag{3.24}$$

$$= \mathrm{Tr}\left(g_1^{\dagger} P_a g_1 \, |\psi\rangle\langle\psi|\right) = \mathrm{Tr}(P_{a+1} \, |\psi\rangle\langle\psi|), \tag{3.25}$$

where we have used the relation [44]:

$$g_1^{\dagger} P_a g_1 = \frac{1}{q} \sum_{j=0}^{q-1} \omega^{-aj} g_1^{\dagger} A^j g_1 = \frac{1}{q} \sum_{j=0}^{q-1} \omega^{-aj} \omega^{-j} A^j = P_{a+1}. \tag{3.26}$$

Thus, $p(a) = p(a+1)$, implying that all q measurement outcomes are equally likely. After the measurement, the anticommuting generator g_1 is removed from $\mathcal{G}$, and A is added instead, ensuring the post-measurement state is stabilized by the measured observable.

In practice, when simulating entanglement scaling transitions in monitored circuits, it is not necessary to track individual measurement outcomes, since all possible outcomes results share the same updated generating set $\mathcal{G}$. This set alone suffices to compute entanglement entropies, as discussed in the following section.

3.5 Rényi entropy in the stabilizer formalism

In Sec. 2.1, we introduced the Rényi entropy, Eq. (2.7), as a one-parameter generalization of the von Neumann entropy. Powers of the bipartite reduced density matrix ρ_A, of subsystem A, serve as its nonlinear arguments. As our model deals exclusively with stabilizer states, Eq. (2.7) can be greatly simplified.

To begin, we express the reduced density matrix ρ_A as a sum over projectors, corresponding to stabilizers strings with nontrivial support strictly in the subsystem A:

$$\rho_A = \mathrm{Tr}_B[\rho] = \frac{1}{2 \cdot q^L} \sum_{s \in A \cup B} \mathrm{Tr}_B[s + s^{\dagger}] = \frac{q^{|B|}}{2 \cdot q^L} \sum_{s \in A}(s + s^{\dagger}) \tag{3.27}$$

$$= \frac{1}{2 \cdot q^{|A|}} \sum_{s \in A}(s + s^{\dagger}). \tag{3.28}$$

Now, we compute the powers of the reduced density matrix ρ_A:

$$\rho_A^2 = \left(\frac{1}{2 \cdot q^{|A|}} \sum_{s \in A}(s + s^{\dagger})\right)^2 \tag{3.29}$$

$$= \frac{1}{4 \cdot q^{2|A|}} \sum_{s,s' \in A}(s + s^{\dagger})(s' + s'^{\dagger}) \tag{3.30}$$

$$= \frac{2|s_A|}{4 \cdot q^{2|A|}} \sum_{s \in A}(s + s^{\dagger}) \tag{3.31}$$

$$= \frac{|s_A|}{q^{|A|}} \rho_A, \tag{3.32}$$

where $|s_A|$ is the size of the stabilizer group supported exclusively on A. This derivation utilizes properties of stabilizer groups over prime-dimensional local Hilbert spaces. Namely, the set of stabilizers generated by $X_{\mathfrak{q}}$ and $Z_{\mathfrak{q}}$, i.e., $\langle X_{\mathfrak{q}}, Z_{\mathfrak{q}} \rangle$, is equal to its adjoint $\langle X_{\mathfrak{q}}^\dagger, Z_{\mathfrak{q}}^\dagger \rangle$. Thus, given stabilizers s, s' supported within A, the products $s \cdot s'^\dagger$ and $s^\dagger \cdot s'$ also lie within the stabilizer support of A. We can now write a recursion:

$$\rho_A^n = \left(\frac{|s_A|}{q^{|A|}} \right)^{n-1} \rho_A. \tag{3.33}$$

Using this recursion, the Rényi entropy takes a particularly simple form:

$$S^n(A) = \frac{1}{1-n} \log_q \left(\mathrm{Tr} \left[\left(\frac{|s_A|}{q^{|A|}} \right)^{n-1} \rho_A \right] \right) \tag{3.34}$$

$$= \frac{1}{1-n} \log_q \left(\left(\frac{|s_A|}{q^{|A|}} \right)^{n-1} \mathrm{Tr}[\rho_A] \right) \tag{3.35}$$

$$= |A| - \log_q |s_A| \tag{3.36}$$

$$= |A| - |\mathcal{G}_A|. \tag{3.37}$$

Here, we have used linearity of the trace, followed by the property that the number of linearly independent stabilizers $|\mathcal{G}_A|$ scales logarithmically with the size of the stabilizer group $|s_A|$ [76]. This expression for the Rényi entropy applies to both periodic and aperiodic systems.

Alternatively, Eq. (3.37) can be derived by directly analyzing the spectrum of ρ_A in Eq. (3.28). For stabilizer states, the entanglement spectrum is flat, meaning all nonzero eigenvalues of ρ_A are equal. Substituting this flat spectrum into the definition of Rényi entropy also reproduces Eq. (3.37).

Chapter 4

Measurement-induced entanglement transitions in $q > 2$

In this chapter we turn our focus to the dynamics of entanglement in a one-dimensional lattice composed of qudits ($q > 2$). While a brief introduction to quantum entanglement in qudits was outlined in Chapter 1, we begin now by reviewing some existing analyses of entanglement transitions in qudit systems. Following the outline of Chapter 2, we then discuss the nature of the growth and thermalization of entanglement under varying local Hilbert space dimensions. Finally, we turn our attention to entanglement scaling transitions, driving by local projective measurements, in these qudit systems.

4.1 Review of entanglement transitions in qudit systems

Following the qubit setting, a growing body of literature has explored measurement-induced entanglement transitions in systems with higher local Hilbert space dimensions, spanning a variety of dynamical frameworks. These include evolution under Haar-random [31, 32], Clifford [37, 38], and Brownian unitaries [39], implemented on various lattice geometries.

On the one-dimensional periodic lattice, the most general case corresponds to evolution under Haar-random unitaries interspersed with local projective measurements. In the qubit case ($q = 2$), this model exhibits a measurement-induced entanglement transition as described in Chapter 2 for the Clifford model, albeit with a different critical measurement rate. For higher local Hilbert space dimensions ($q > 2$), the transition retains the same universal exponents as observed in the qubit setting [31]. In the limit of an infinite-dimensional local Hilbert space, the transition maps onto the two-dimensional bond percolation problem, which has a critical point at $p_c = 1/2$ [32]. From the perspective of quantum error correction, the persistence of volume-law entanglement despite the non-local disentangling action of measurements can be interpreted as an instance of fault tolerance [40]. This viewpoint facilitates the derivation of an upper bound on the critical measurement rate at which the entanglement scaling transition occurs:

$$p_c \, \log[(q^2 - 1)(p_c^{-1} - 1)] \leq \log[q(1 - p_c)]. \tag{4.1}$$

For $q = 2$ this bound validates the critical point occurring at 0.16 and in the limit $q \to \infty$ it bounds $p_c \leq 1/2$ [40]. The purification transition, wherein local projective measurements drive the purification of a mixed-state density matrix, has been shown to share the critical measurement rate with the entanglement scaling transition. Notably, however, the entanglement transition is absent when projective measurements are performed in arbitrary non-local bases [32]. Moreover, when dissipative processes are introduced at the system boundary, measurements have been shown to aid in maintaining the purity of the state [41]. This behaviour arises because local measurements curb the support of stabilizers strings. This ensures that

the stabilizer supports do not reach the dissipative boundary, and the pure state is preserved.

Recent studies have investigated entanglement scaling transitions in monitored qudit Clifford circuits, revealing results that overlap with those presented in this chapter [37, 38]. As this overlap came to our attention only after the completion of our investigation, we provide a brief review of these developments here. In Ref. [37], a numerically-driven analysis investigates the critical behavior of the entanglement transition at higher local Hilbert space dimensions. Using Rényi entropies in the stabilizer formalism (Sec. 3.5), the study demonstrates a convergent increase in the critical measurement rate, alongside a Hilbert-space-dimension-invariant correlation length exponent close to that of the bond percolation transition. Building on this, Ref. [38] constructs an analytically tractable statistical model to describe the critical properties of monitored Clifford circuits. Within this statistical model, the symmetries of the Boltzmann weights reveal that the universal exponents at each finite local Hilbert space dimension $d = q^m$ depends solely on the underlying prime q. In the infinite-dimensional limit, the Clifford model once again maps onto the bond percolation transition, mirroring the Haar-random case. Furthermore, the critical measurement rate and the universal exponents remain robust under perturbations in the evolution. A similar entanglement scaling transition is observed in two-dimensional random tensor network models under Clifford evolution [42]. Herein, the boundary entanglement entropy exhibits a transition from volume-law to area law scaling, tuned by the rate of elimination of virtual bonds in the system's bulk. For prime virtual bond dimensions, a convergent critical elimination rate is observed, with critical properties again determined by the base prime dimension, consistent with the behavior found in monitored Clifford circuits [38].

Finally, despite the conceptual simplicity offered by one-dimensional lattices, they typically necessitate deep circuits to observe the entanglement scaling transition of thermal entanglement entropies. As an alternative, two-dimensional brickwork circuits with shallow depth have been proposed [43]. Such a model demonstrates that measurements performed in the bulk can moderate the entanglement phase at the boundary of the system. A convergent increase in the critical measurement probability with increasing local Hilbert space dimension is observed in this case as well.

4.2 Entanglement growth in qudit Clifford circuits

First, we consider the dynamics of entanglement growth under unitary evolution generated by two-qudit Clifford gates, following the layered brickwork structure illustrated in Fig. 2.2. The one-dimensional lattice is initialized in the vacuum state, $|0\rangle^{\otimes L}$, and the entanglement is quantified using the Rényi entropy defined in Eq. (3.37). As observed in the qubit case, the entropy rapidly attains its thermal value in $O(L)$ time steps, as shown in Fig. 4.1. However, with increasing local Hilbert space dimension, the entanglement appears to spread more rapidly. The entanglement velocity v_E increases convergently. The observed values of v_E, up to $q = 13$, are summarized in Table 4.1, and the limit $q \to \infty$ is discussed in Sec. 5.2.

This increase in v_E can be understood by considering the support of qudit Clifford unitaries. The number of two-qudit Clifford unitaries that act nontrivially on both qudits scales quadratically with the Hilbert space dimension, as $O(q^2)$, whereas the number of single-qudit-support unitaries scales linearly, as $O(q)$. We refer to the former as *support-broadening* Clifford unitaries and the latter as *support-diminishing* unitaries. Support-broadening unitaries tend to preserve or increase entanglement between qudits. While such unitaries can,
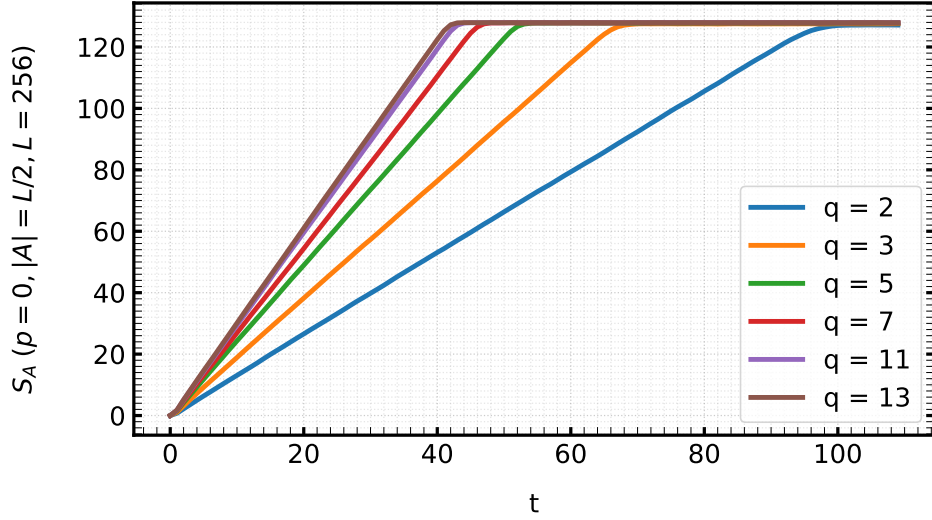
Figure 4.1: Entanglement growth under unitary evolution with two-qudit Clifford gates, for varying local Hilbert space dimensions q. The entanglement spreading velocity v_E, extracted from the prethermal slope of entanglement growth, shows a convergent increase.

in principle, result in disentangling dynamics, these scenarios are sparse, as previously discussed in the qubit case in Ref. [34]. An interesting direction for further investigation would be to characterize the spectrum of entanglement structures in one-dimensional qudit systems, and to determine whether unitaries can be constructed to systematically disentangle these structures in higher Hilbert space dimensions.

q	v_E	B
2	1.314 ± 0.002	0.125 ± 0.027
3	1.916 ± 0.002	-0.045 ± 0.023
5	2.469 ± 0.002	-0.167 ± 0.026
7	2.809 ± 0.008	-0.626 ± 0.074
11	3.003 ± 0.006	-0.210 ± 0.052
13	3.096 ± 0.006	-0.347 ± 0.049

Table 4.1: Fitted values of the entanglement velocity v_E and the nonuniversal constant B for different prime local Hilbert space dimensions q, obtained by fitting the KPZ form of mean entropy growth (Eq. (2.10)) using least-squares regression. Errors are reported up to two standard deviations.

4.3 Generalization of measurement-induced entanglement transitions

Now, we generalize measurement-induced entanglement transitions by incorporating local projective measurements in random unitary circuits composed of two-qudit Clifford unitaries. These measurements are performed in the computational basis, using projectors which correspond to the eigenvalues of the generalized $Z_\mathfrak{q}$ operator. The system is initialized in the vacuum state $|0\rangle^{\otimes L}$, and measurements are applied to each qudit independently with a finite probability, as shown in Fig. 2.3. We have investigated the measurement-induced transition for prime local Hilbert space dimensions up to $q = 13$. Thus, we extend the analysis of the entanglement scaling transition discussed for qubits in Chapter 2, and put forth conjectures regarding the general behavior of these transitions in higher-dimensional systems.

As in the qubit case, introducing measurements suppresses the thermal value of the entanglement entropy. Higher measurement rates correspond to lower entanglement entropy at long times, as illustrated for $q = 3$ and $q = 5$ in Fig. 4.3a. One must note that the entanglement entropy is calculated as an ensemble of circuit trajectories, each initialized identically and subjected to the same measurement rate. This averaging procedure eliminates any artifacts arising from the circuit configuration in the entropy growth and thermalization, and ensures that the measurement rate is the sole parameter controlling the phase transition. It is also important to note that, for a given qudit dimension, the time to reach thermalization in such brickwork circuits is determined solely by the system size and remains independent of the measurement rate. However, for different unitary configurations in the circuit, or for open-boundary conditions, the thermalization time may vary.

As discussed in the previous section, an increase in the local Hilbert space dimension q leads to a monotonic increase in the proportion of Clifford unitaries that broaden the support of the stabilizer generators. Consequently, for a fixed measurement rate p between Hilbert space dimensions, systems with larger q exhibit higher steady-state entanglement entropy $S_A(p)$, as shown in Fig. 4.3a.

This shift in steady-state entropies directly influences the critical measurement rate p_c at which the entanglement scaling transition occurs. The critical measurement rate p_c increases with the local Hilbert space dimension. Despite this shift, the features of the transition remain preserved: in the volume law regime, the entropy scales linearly with subsystem size, while in the area law regime, it saturates to a constant, and at criticality, a characteristic logarithmic scaling is observed (Fig. 4.3b). For $q = 3$ and $q = 5$, the critical measurement rates are estimated to be $p_c^{\mathfrak{q}=3} \approx 0.28$ and $p_c^{\mathfrak{q}=5} \approx 0.38$, respectively, as shown in Fig. 4.3c.

Additional insight into the shift in criticality is provided by the mutual information $I(A : B)$, computed as detailed in Chapter 2, and shown in Fig. 4.4. Mutual information is exponentially suppressed in both the area and the volume-law regimes [117]. However, near the critical point, long-range correlations supported exclusively within the partitions A and B become significant, resulting in a peak in $I(A : B)$. These peaks are independent of the system size, and their saturation heights are governed by an emergent conformal field theory (CFT) at criticality [29]. As shown in Fig. 4.4, the critical measurement rate p_c grows with q and appears to asymptotically approach $p_c \approx 1/2$ as $q \gg 1$. While our simulations extend up to $q = 13$, previous works suggest that in the limit $q \to \infty$, the monitored Haar-random circuit model is described by classical two-dimensional bond percolation [32, 118], which features a critical points at $p_c = 1/2$. This limiting value is also consistent with the

| q	a_{p_c}	p_c	ν
2	1.49 ± 0.04	0.16	1.298
3	0.95 ± 0.03	0.28	1.387
5	0.67 ± 0.04	0.38	1.398
7	0.86 ± 0.05	0.41	1.29
11	0.96 ± 0.05	0.44	1.323
13	0.87 ± 0.05	0.45	1.343

Table 4.2: Summary of critical properties of the measurement-induced entanglement transition up to $q = 13$, including: the logarithmic coefficients of the entropy growth at criticality (α_{p_c}); the critical measurement rates p_c, which approach 0.5 as $q \to \infty$; and the correlation length exponent ν, which remains close to its classical two-dimensional bond percolation counterpart, $\nu_{\mathrm{cl}} = 4/3$.

analytical upper bound in Eq. (4.1). A summary of the converging critical points is provided in Table 4.2. Additionally, we note that Ref. [38] extends this numerical analysis to higher prime q, which show a slow but persistent convergence toward this limit.

Finally, we revisit the scaling of entanglement entropy at criticality. Similar to the qubit case, the entanglement entropy at $p = p_c$ exhibits logarithmic growth with both the sub-system size and time during thermalization [29]. The time-dependent logarithmic growth is displayed in Fig. 4.2, and the corresponding coefficients extracted for various studied values of q are summarized in Table 4.2.
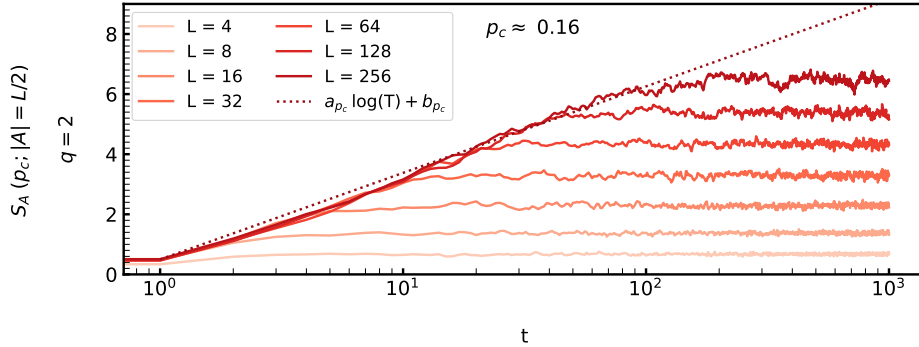
Figure 4.2: At the critical measurement rate, the entanglement entropy exhibits logarithmic growth, following Eq. (2.12). The coefficients of the logarithmic scaling behavior, α_{p_c}, are summarized in Table 4.2.

(a)

(b)

(c)
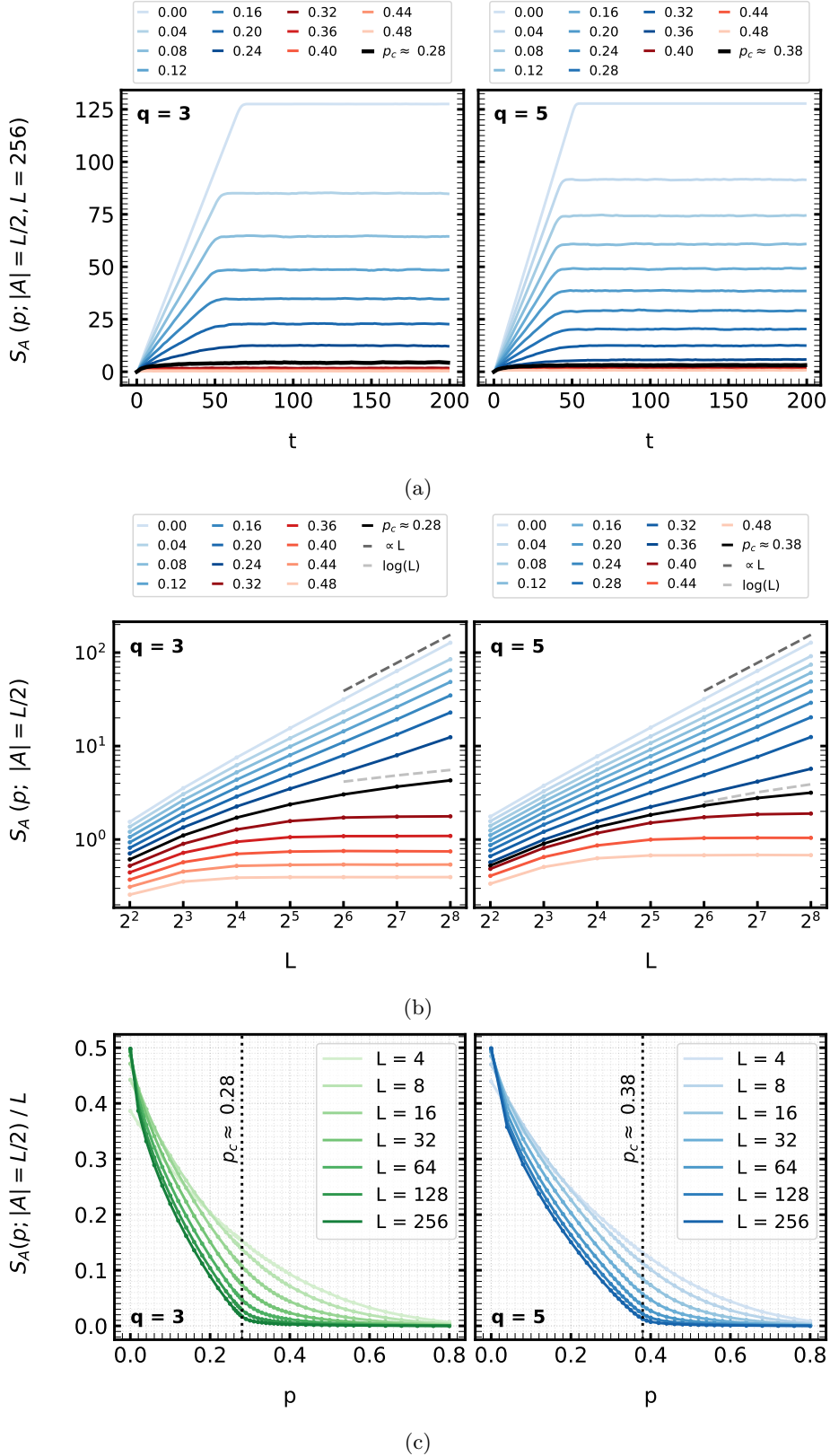
Figure 4.3: Measurement-induced entanglement transition in Hilbert space dimensions $q = 3, 5$, compared to the qubit case discussed in Chapter 2. The entanglement growth (a) and the thermal entropy scaling (b) closely resemble the qubit case, demonstrating a transition from a volume-law regime (blue) to an area-law regime (red), with logarithmic scaling at the critical measurement rate p_c. The rescaled entropy S_A/L (c) serves as an order parameter that vanishes in the area-law regime, indicating the shift of the critical measurement rates.
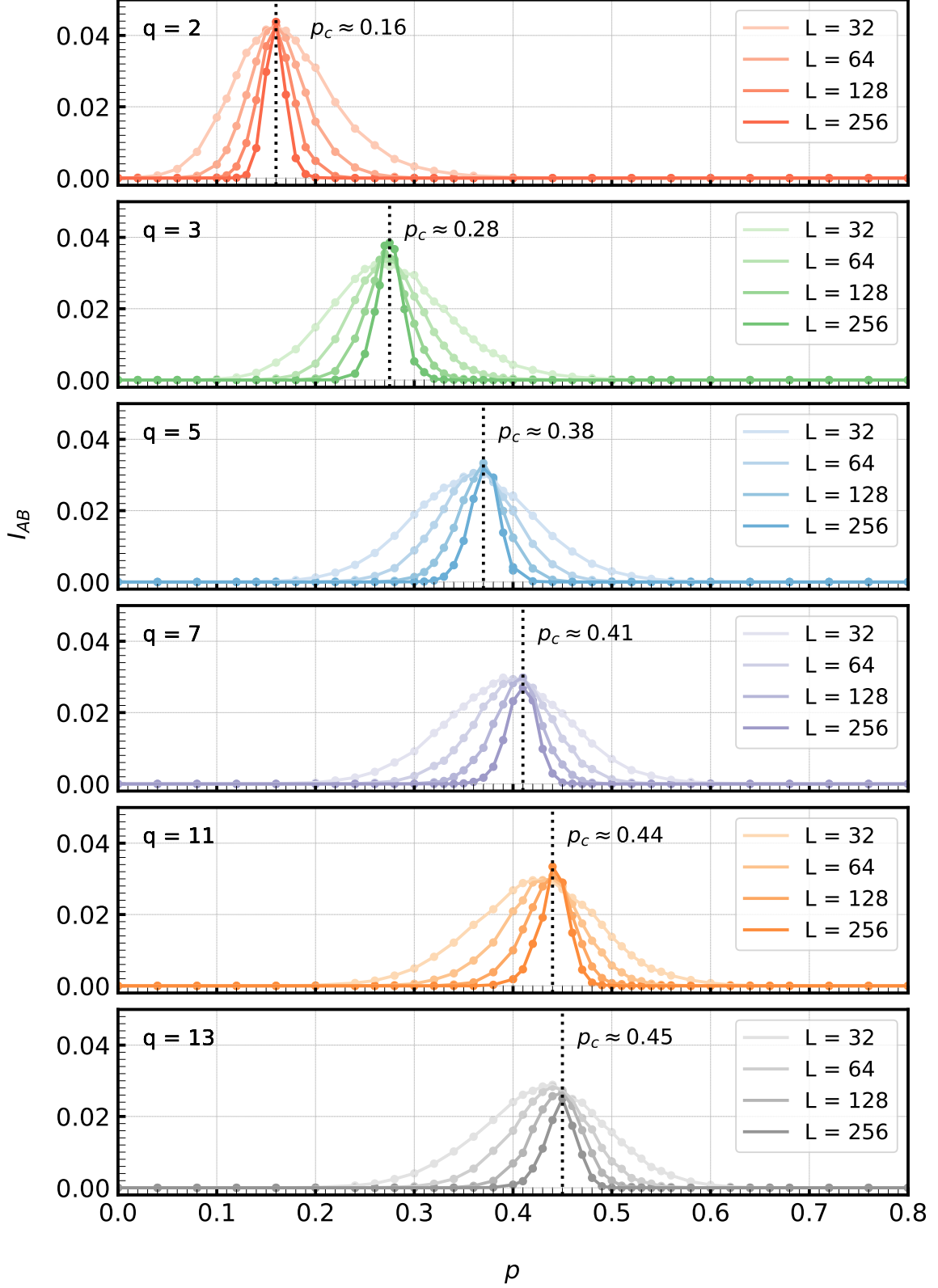
Figure 4.4: The disjoint mutual information (Eq. (2.8)) provides more precise estimates of the critical measurement rates, exhibiting sharper peaks that saturate to a constant in the thermodynamic limit. A comparison across different local Hilbert space dimensions q shows that the critical point increases, and converges towards $1/2$ as $q \to \infty$.

4.4 Universality across Hilbert space dimensions

Next, we attempt to characterize the measurement-induced entanglement transition by extracting critical exponents. To do so, we perform a finite-size scaling analysis of the observables studied thus far: the bipartite thermal entanglement entropy and the Rényi mutual information. Finite-size scaling allows us to analyze the nature of observables across the parameter space while circumventing finite-size effects. This method is instrumental in detecting and characterizing continuous phase transitions and the universal properties emerging at criticality. To circumvent finite-size effects, one selects a scaling form such that the observable values, when appropriately rescaled, collapse onto a single universal curve across different system sizes. In the study of measurement-induced entanglement transitions, the choice of the scaling form is not unique and can affect the extracted critical exponents [29, 79]. Here, we utilize the scaling form proposed in Refs. [117, 119]:

$$S_A(p, L, |A| = L/2) = \delta(p_c) \log(L) + \mathrm{G}(L/\xi), \tag{4.2}$$

$$|S_A(p, L, |A| = L/2) - S_A(p_c, L, |A| = L/2)| = \tilde{\mathrm{G}}((p - p_c)L^{1/\nu}), \tag{4.3}$$

where $\delta(p_c)$ is the coefficient of the logarithmic scaling of the entropy with subsystem size, and $G(L/\xi)$ is a universal function of the rescaled system size.

Equation (4.2) can be motivated directly from the scaling of the entanglement entropy with the subsystem size, presented in Eq. (2.12). Alternatively, it can be heuristically constructed by analogy with two-dimensional bond percolation [117]. In particular, Ref. [117] demonstrates that the quantification of the Hartley entropy of a monitored Haar random quantum circuit can be mapped onto the problem of counting the minimum number of bonds that must be traversed, or *cut*, on a two-dimensional percolation lattice. In this mapping, a weak measurement rate corresponds to a lattice with relatively few broken bonds, and hence the number of cuts made grows linearly with system size. Conversely, at strong measurement rates, an ample proportion of broken bonds permit free passage across the lattice. At the critical measurement rate, the number of cuts grows logarithmically with system size. Thus, the logarithmic term in Eq. (4.2) captures the critical scaling behavior of the entanglement entropy. Subtracting this critical logarithmic term isolates the scaling function $\tilde{G}((p - p_c)L^{1/\nu})$ in Eq. (4.3), where ν is critical exponent of the correlation length:

$$\xi = \frac{1}{|p - p_c|^\nu}. \tag{4.4}$$

The results of this scaling analysis are shown in Fig. 4.5 for local Hilbert space dimensions $q = 2, 3, 5$. For qubits ($q = 2$), the correlation length exponent ν has been reported to be approximately 1.3 [29], close to the classical two-dimensional percolation value $\nu = 4/3$. We find that ν remains close to its classical counterpart across different local Hilbert space dimensions, as summarized in Table 4.2. While the emergence of percolation-like behavior is formally expected only in the limit of infinite local Hilbert space dimension [32, 40], the apparent invariability of ν with q is notable.

While there isn't a standard strategy to obtain the scaling collapse, we follow the procedure outlined in Ref. [117], and briefly summarize the method here. By utilizing the datapoints (p, L) of the observables, we construct the rescaled variable $x(p, L) = (p - p_c)L^{1/\nu}$, and define the shifted curves $y_L(x) = S(p, L) - S(p_c, L)$ for each system size L. Following Eq. (4.3), these curves are now centered at the critical point p_c, whose initial estimated is obtained

from the peaks of the mutual information. Interpolations between the data points are used to smoothly define $y_L(x)$. To optimize the quality of the collapse, we define the objective function

$$R = \sum_{i,L} \left[y_L(x_i) - \bar{y}(x_i) \right]^2 , \qquad (4.5)$$

where $\bar{y}(x_i)$ denotes the mean value of $y_L(x_i)$ across all system sizes. Hence, the objective function represents the sum of the mean squared deviations from the mean curve. We also constrain the critical point p_c to vary within a narrow window around the initial mutual information estimate. Finally, by minimizing $R(p_c, \nu)$, we then extract optimal estimates for (p_c, ν) for each Hilbert space dimension.
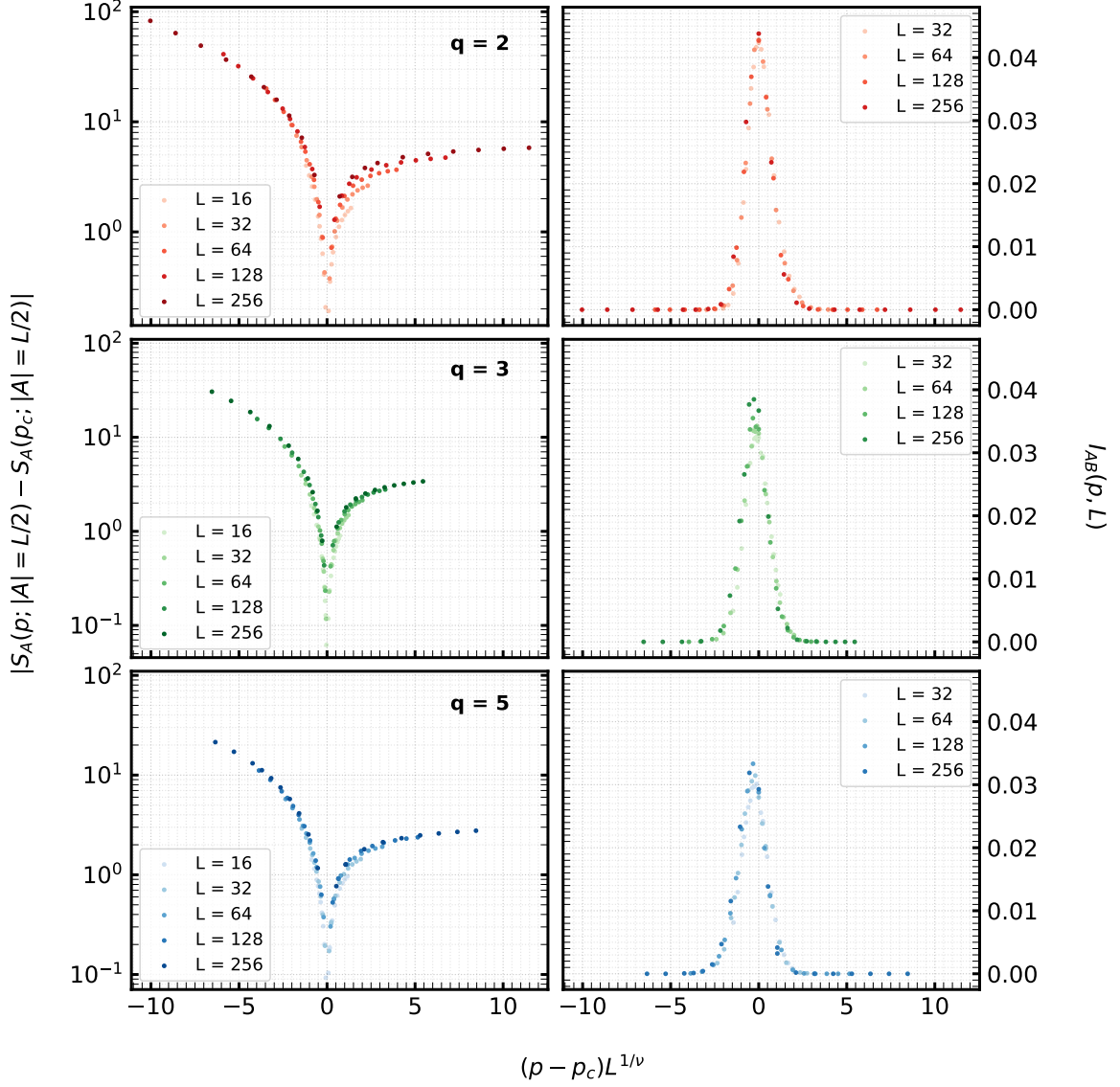
Figure 4.5: Data collapse of the steady-state entanglement entropy (left) and the Rényi mutual information (right) for local Hilbert space dimensions $q = 2, 3, 5$, plotted against the rescaled variable $x = (p - p_c)L^{1/\nu}$. The steady-state entanglement entropy is computed for a subsystem of size $L/2$, and the mutual information for two diametrically opposite subsystems of size $L/8$. Both observables exhibit a scaling collapse for a critical exponent $\nu \approx 1.3$, consistent across q, at the respective critical measurement rates listed in Table 4.2.

Chapter 5

Entanglement dynamics in the limit $q \to \infty$

The extension of the measurement-induced entanglement transition to higher local Hilbert spaces calls for the study of both the universality of the transition, and the behavior in the limiting case $q \to \infty$. While the recent work Ref. [38] formulates a general statistical framework to investigate universality and the conformal properties of the critical point, here we focus on the infinite local Hilbert space limit. In this section, we introduce a simplified representation of stabilizer states, which enables the construction of a minimal dynamical model capturing the growth and thermalization of entanglement entropy under two-qudit Clifford unitaries in the large-q limit. Although minimal models have been explored in this limit before, the framework we propose offers a new insight into the entanglement structure of one-dimensional qudit lattices.

5.1 Clipped gauge of the stabilizer representation

Our numerical simulations rely crucially on the stabilizer formalism introduced in Chapter 3, which enables efficient representation of pure quantum states using $O(L)$ linearly independent stabilizers group generators, each of length $2L$, organized in the stabilizer tableau. However, even when global phases are excluded, the generating set of stabilizers $\mathcal{G}$ is not unique. The exponential cardinality of the stabilizer group permits many linearly independent subsets to generate the full stabilizer group. This degree of freedom in the stabilizer representation is interpreted as a gauge ambiguity. To glean any structural properties from the stabilizer tableau, this gauge ambiguity needs to be resolved. Ref. [76] introduced a two-step row reduction procedure on the stabilizer tableau to perform the gauge-fixing. Herein, the generating set undergoes a minimization of the support of each stabilizer, thereby *clipping* each stabilizer.

The clipping procedure relies on the explicit definitions of the left and right endpoints of a stabilizer generator g, denoted $\ell(g)$ and $r(g)$, respectively. These correspond to the leftmost and rightmost lattice sites where the operator g acts nontrivially. Based on this, we define the endpoint distributions $\rho_\ell(x)$ and $\rho_r(x)$ as the densities of stabilizer endpoints at position x for the left and right endpoints, respectively. The *clipped gauge* is then characterized by two constraints [76]:

- At each site x, $\rho_\ell(x) + \rho_r(x) \leq 2$; equality holds for pure states.

- If $\rho_\ell(x) = 2$ (or $\rho_r(x) = 2$), the two stabilizers operators acting at site x must be linearly independent, i.e., they anticommute locally at site x.

These conditions are valid for arbitrary prime local Hilbert space dimensions. However, *clipping* itself does not uniquely determine the contents of $\mathcal{G}$, instead, it fixes the stabilizer lengths. Particularly, for any complete set of stabilizers generators $\{g_i\}_L$ for a state

$|\psi\rangle$, the imposition of the clipped gauge returns the same set of endpoints $\{\ell(g_i), r(g_i)\}$. This gauge-fixing grants us access to the distribution of stabilizer string lengths, which encodes information about the structure of entanglement, and also serves as a marker for the measurement-induced entanglement transition [29].

Now, we describe how to implement the clipping and compute entanglement entropy within it. The clipping procedure comprises of two row reduction subroutines on the stabilizer tableau [29], which leverage the cyclic structure of prime-dimensional finite field arithmetic. The first row reduction targets the left endpoint distribution $\rho_\ell(x)$ and implicitly enforces the clipped gauge condition. In the stabilizer tableau, the linearly independent generators of the generalized Pauli group, $X_{\mathfrak{q}}$ and $Z_{\mathfrak{q}}$, are stored in separate columns for each lattice site x. Performing a standard row reduction brings the tableau into row echelon form, ensuring that if two stabilizers share the same left endpoint at site x, they are linearly independent. The second row reduction is applied to the right endpoints. To preserve structure of the first reduction, the tableau is first vertically flipped to order the stabilizers by descending left endpoints, i.e., $\ell(g_i) \geq \ell(g_j)$ for any ordered pair $i < j$. This ensures that the second reduction does not interfere with the clipped structure of the left endpoints. After both reductions are performed, the endpoint distributions $\rho_\ell(x)$ and $\rho_r(x)$ satisfy the clipping constraints.

The clipped gauge allows the reformulation of the entanglement entropy. In Eq. (3.37), the Rényi entropy is determined by the number of linearly independent stabilizer generators $|\mathcal{G}_A|$ supported entirely within a subsystem A. In the absence of gauge-fixing, consider a simple multiplicative combination of two stabilizer strings of the form $g_3 = g_1 \cdot g_2$. Since the right endpoint of g_1 and g_2 can be linearly dependent, such as $X_{\mathfrak{q}}^\alpha$ and $X_{\mathfrak{q}}^{q-\alpha}$, the product stabilizer g_3 can have a smaller support than its factors g_1 and g_2. The clipped gauge eliminates this occurrence by imposing linear independence on the endpoints. If $\ell(g_1) = \ell(g_2)$, then $\ell(g_3) = \ell(g_1)$, while $\alpha \neq q$. For a contiguous subsystem A, the number of linearly independent stabilizer generators $|\mathcal{G}_A|$ simply becomes the number of stabilizers which have both endpoints in the biparition A.

With this consideration, to compute the Rényi entropy for a periodic, contiguous bipartition A, or equivalently the entropy of its complement $\overline{A}$, we classify stabilizers by their endpoints relative to A: stabilizers with both endpoints in A (n_{in}^A), stabilizers with both endpoints outside A ($n_{\text{out}}^A = n_{\text{in}}^{\overline{A}}$) and stabilizers with one end point in both A and $\overline{A}$ (n_{cut}^A). Since $|\mathcal{G}_A| = n_{\text{in}}^A$ and the clipped-gauge for pure states enforces $2|A| = 2n_{\text{in}}^A + n_{\text{cut}}^A$, the Rényi entropy can be reformulated as

$$S_A = |A| - |\mathcal{G}_A| = n_{\text{in}}^A + \frac{1}{2}n_{\text{cut}}^A - n_{\text{in}}^A = \frac{1}{2}n_{\text{cut}}^A. \tag{5.1}$$

Hence, the bipartite entropy is simply half the number of clipped-gauge stabilizers with one endpoint in A and the other in $\overline{A}$.

5.2 Unitary dynamics in the clipped gauge

In this section, we focus on the limit $q \to \infty$, and analyzing the action of two-qudit Clifford unitaries from the lens of the clipped-gauge representation. In this limit, we show that action of random Clifford unitaries converges to a *classical limit*. The clipped gauge, in addition to

being an additional tool to access the entanglement transition [29], can be employed to elicit the entanglement structure of a quantum state from its stabilizer generators [34].

In constructing this framework, we follow the approach of Ref. [76], which maps entanglement growth under random circuits to an operator spreading problem. In doing so, Ref. [76] demonstrates captures emergent KPZ dynamics by tracking solely the endpoints of stabilizer generators in the clipped gauge. We build on this approach, by keeping a track of the identity of the stabilizer generators to which the endpoints belong. In doing so, we omit the information about the contents of the stabilizer generators. As a result, we represent the stabilizer tableau as a simple graph, where the edges encode the entanglement structure between qudits. By analysing the convergent behaviour of Clifford unitaries in the limit $q \to \infty$, introduced ahead, we obtain an effective visualization of the entanglement structure and dynamics in the large Hilbert space limit $q \gg 1$. One must note that this representation is distinct from the standard equivalence between the stabilizer representations and graph states. Furthermore, the entropy profile of a quantum state, defined by computing the entanglement entropies across all possible bipartitions of the system, can uniquely characterize quantum states. However, constructing such an entropy profile is computationally demanding. Instead, this graph-based representation of the clipped stabilizer generators offers a numerically efficient means to characterize individual states.

To incorporate unitary dynamics within this graph-based representation, we first analyze the behavior of Clifford unitaries in the large-q limit. This analysis draws on the notions of support-broadening and support-diminishing unitaries introduced in Chapter 4. Briefly, the number of two-qudit Clifford unitaries that act non-trivially on both of their constituent qudits scales as $O(q^2)$, whereas those acting non-trivially on only one qudit scale as $O(q)$. Consequently, in the limit $q \to \infty$, almost all unitaries belong to the support-broadening class, i.e., they form a full-measure set.

To understand the action of these unitaries on clipped-gauge stabilizer generators, we conducted an extensive numerical study of their action on stabilizer states in the absence of clipping, and analyzed the resulting entropy profiles. Summarizing our results in the graph-based representation, we find that two-qudit support-broadening unitaries in the large-q limit act to rearrange the connections between the two involved nodes in a way that maximizes the local entanglement. That is, among all possible post-unitary configurations, the resulting local graph structure corresponds to the one that maximizes the entanglement entropy across all bipartitions of the one-dimensional chain. Hence, the Clifford unitaries demonstrate a scrambling action to maximize entropy growth at each step.

An illustrative example can provided by a simple three-qudit circuit undergoing two steps of evolution, depicted in Fig. 5.1. The initial state is a product state described by three stabilizers with local support. After the first unitary, there are two potential outcomes: one where the product state is preserved, and another where the first two qudits share one unit of entanglement, as measured by Eq. (5.1). In the large-q regime, the entangled configuration is the dominant outcome amongst all two-qudit unitaries. The second unitary, acting on the second and third qudits, produces three possible outcomes: two in which one qudit remains disentangled from the rest, and a third corresponding to an multipartite entangled three-qudit state. Once again, the entanglement maximizing configuration emerges as the dominant result. In the strict limit $q \to \infty$, the probability of obtaining this highly entangled outcome approaches unity, yielding a deterministic classical description of the dynamics. For large but finite $q \gg 1$, the locally disentangled outcomes persist only with a vanishingly

small probability. This behavior highlights the strong statistical bias towards the generation of multipartite entangled states under the support-broadening action of Clifford unitaries in the infinite-dimensional Hilbert space limit.
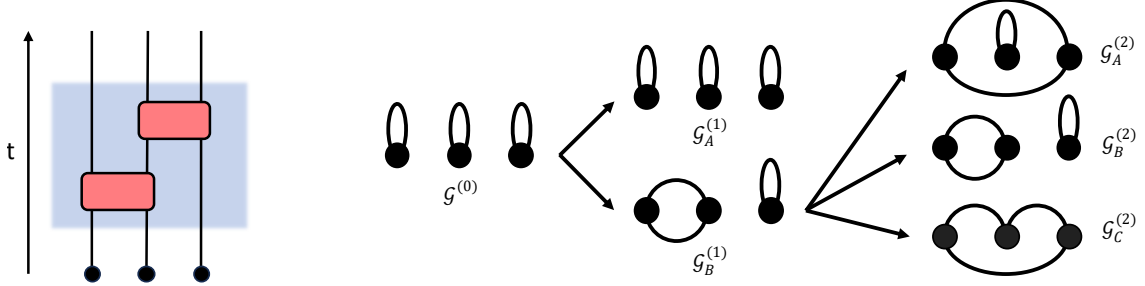
Figure 5.1: Illustration of the evolution of a clipped-gauge stabilizer state in the large-q limit. The circuit (left) applies a unitary on qudits 1 and 2, followed by a unitary on qudits 2 and 3. After each unitary, the stabilizer state transforms to the configuration that maximizes the entanglement entropy across all bipartitions. The resulting states after the first and second unitary actions are $\mathcal{G}_B^{(1)}$ and $\mathcal{G}_C^{(2)}$, respectively.

For relatively small system sizes as the illustration above, it is feasible to enumerate all possible outcomes of local unitary actions and directly inspect the stabilizer tableau to identify the configuration that maximizes the entanglement entropy across all bipartitions. However, such a brute-force approach quickly becomes impractical as we scale toward larger systems, as we typically seek to compute observables towards the thermodynamic limit. To bypass these extensive computations of entanglement entropy, we formulate a simple set of rules that govern the evolution of the graph configurations under two-qudit Clifford dynamics in the $q \to \infty$ limit.

We identify six distinct types of local configurations that can exist prior to the application of a unitary, each corresponding to a different entanglement structure between the two involved qudits and the remainder of the one-dimensional lattice. The graph transformations under unitary evolution are described below. We begin by considering the two simplest cases, illustrated in Fig. 5.2, both of which appeared in our earlier example. In the first case, the unitary acts on a product state of two locally supported qudits. As $q \to \infty$, the dominant outcome is a two-qudit entangled state with one unit of shared entanglement. In the second case, the unitary acts on a pair of qudits that are already isolated from the rest of the system and share one unit of entanglement. Here, the qudits remain entangled, sharing one unit of entanglement.
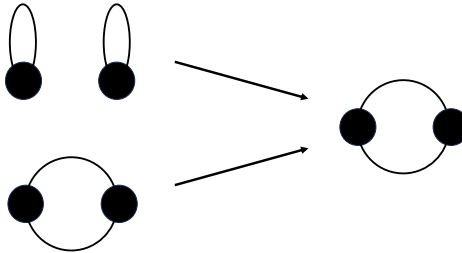
Figure 5.2: Two-qudit clipped-gauge configurations that transform into an isolated two-qudit entangled state under the action of a unitary, in the limit $q \to \infty$.

We now consider the next three cases. These cases can be grouped together as in each of these cases, there exist two clipped-gauge stabilizer generators supported beyond the two qudits upon which the unitary acts, as shown in Fig. 5.3. We denote these generators as g_1 and g_2, and, without loss of generality, assume that $r(g_1) \geq r(g_2)$, meaning the right endpoint of g_1 lies to the right of that of g_2. Upon the action of the unitary, the graph configuration maximizing the entanglement entropy is attained when the two qudits share half a unit of entanglement, i.e., one stabilizer generator forms an edge between the two qudit nodes, and the generators g_1 and g_2 *intersect* in the clipped gauge representation. Concretely, the latter requires that the left endpoint of g_1 shifts to the second qudit and that of g_2 to the first qudit, such that $\ell(g_1) > \ell(g_2)$.
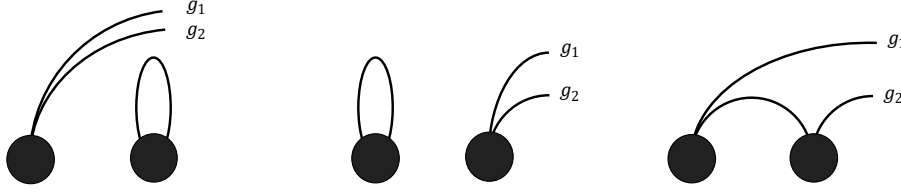
Figure 5.3: Two-qudit clipped-gauge configurations in which any two stabilizer generators extend beyond the site of unitary action.

The final case arises when neither of the two qudits involved has a local support, nor do they support any clipped stabilizers amongst themselves. This configuration, illustrated in Fig. 5.4, consequently involves four clipped-gauge stabilizer generators extending from the two qudits. We denote these generators as g_1, g_2, g_3, and g_4, with the convention that $r(g_1) \geq r(g_2)$ and $r(g_3) \geq r(g_4)$. Additionally, we assume that (g_1, g_2) terminate on the first qudit, i.e., $\ell(g_1) = \ell(g_2) = 1$, and (g_3, g_4) have their left endpoints on the second qudit. In this case, the entanglement-maximizing configuration depends on the initial relative positions of the right endpoints of the four generators. Hence, we branch the protocol into three well-defined sub-cases:
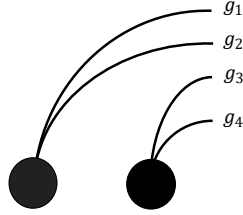
Figure 5.4: Two-qudit clipped-gauge configuration in which all four stabilizer generators extend beyond the site of unitary action.

- **No initial intersections:** As illustrated in Fig. 5.5(a), if there are no intersections among the four stabilizers prior to the unitary action, the entanglement-maximizing configuration is obtained by performing a SWAP operation. The SWAP exchanges the left endpoints of g_1 and g_2 with those of g_3 and g_4.

- **All stabilizers maximally intersect:** In the scenario depicted in Fig. 5.5(b), if each of the four stabilizers intersects with the two stabilizers stemming from the opposite qudit, the initial configuration is already maximally entangled and remains invariant under the unitary action.

- **General case:** In all other configurations conforming to Fig. 5.4, the optimal post-unitary state is the one that maximizes the number of intersections among the four stabilizers. This is achieved by rearranging the left endpoints such that the shorter stabilizer on the second qudit (g_4) is moved to the first qudit ($\ell(g_4) = 1$), and the longer stabilizer on the first qudit (g_1) is moved to the second qudit ($\ell(g_1) = 2$).

(a)   (b)
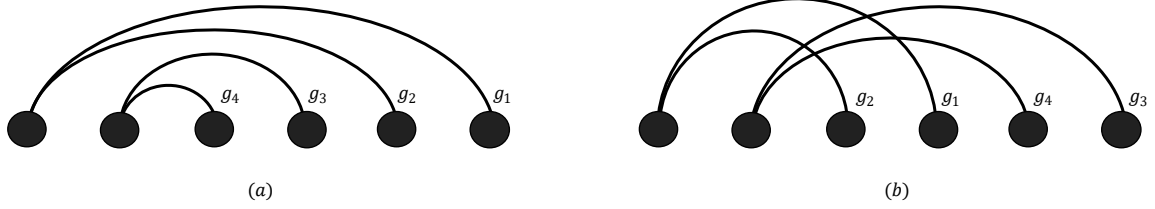
Figure 5.5: Trivial cases of two-qudit clipped-gauge configurations where all four stabilizer generators extend beyond the site of unitary action. (a) No initial intersections between stabilizer generators: the unitary acts as a SWAP operation, (b) maximal intersections between stabilizer generators: the unitary leaves the clipped-gauge generators unchanged.

With this framework, we now have the necessary tools to perform Clifford unitary evolution exactly in the limit of infinite local Hilbert space dimension. To benchmark the accuracy of this graph-based, clipped-gauge evolution model, we compare it to the well-known classical surface growth model introduced in Ref. [76], which employs a set of simple construction rules to model the growth of bipartite entanglement entropies and identifies emergent KPZ universality. We find that the entropy growth and thermalization behavior in our model is identical to that of Ref. [76].

Specifically, the model in Ref. [76] represents bipartite entanglement growth by unit-height blocks lying on the bonds between qudits, with open boundary conditions. Hence, unitary action results in a growing surface, thereby providing an intuitive description of entropy dynamics. In contrast, our graph-based approach permits us to analyze the entanglement structure on the one-dimensional lattice. Specifically, it allows us to identify qudits which share entanglement, distinguish clusters of entangled sites, and track regions of purely local support. While the surface growth model is computationally more efficient and well-suited for global descriptions of entropy growth, our method offers a more detailed description of the underlying entanglement structure. It is also interesting to note that the model in Ref. [76] employs Haar-random unitaries. Hence, our results suggest that in the $q \to \infty$ limit, unitary Clifford dynamics converge with their Haar-random counterparts.

Upon imposing periodic boundary conditions, we fit the entanglement growth curve to the KPZ scaling form, Eq. (2.10), to extract the entanglement spreading velocity v_E and the non-universal constant B. In accordance with the convergent growth trend of v_E presented in Table 4.1, we find $v_E(q \to \infty) = 4.054 \pm 0.004$ and $B(q \to \infty) = -1.148 \pm 0.028$, with errors reported to within two standard deviations.

In a purely unitary random Clifford circuit, the system is expected to evolve toward a steady state that is maximally entangled. Within the graph-based clipped-gauge formalism described above, this steady state is characterized by stabilizer generators of length approximately $L/2$. Specifically, for one-dimensional lattices composed of an even number of qudits, each stabilizer generator is supported over exactly $L/2$ sites. For odd-length chains, all but one stabilizer have length $\lfloor L/2 \rfloor$, and a single generator spans the entire system with length L. This structure naturally emerges from the behavior of stabilizer length distributions as a
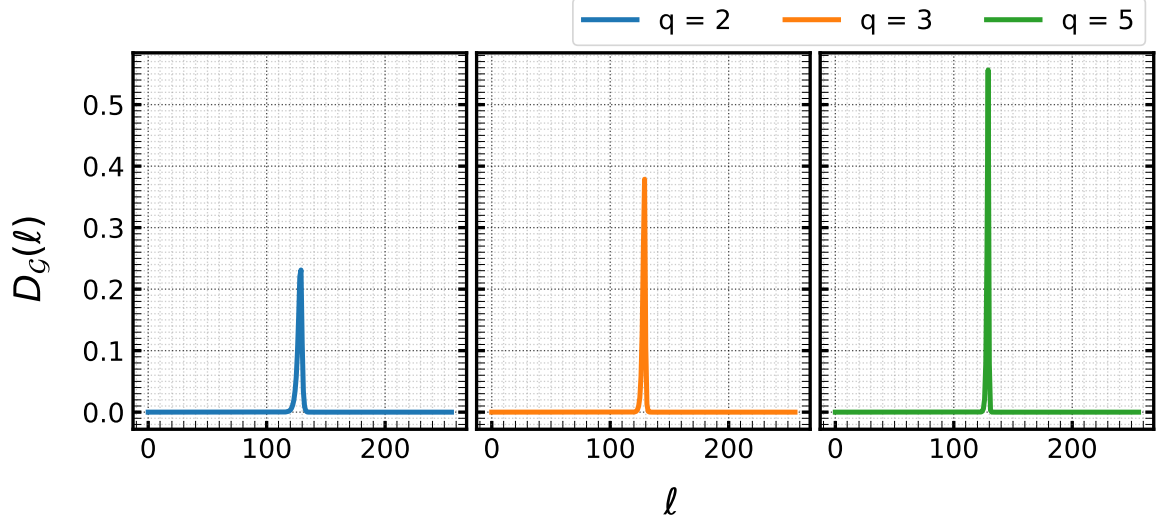
Figure 5.6: Steady-state stabilizer length distributions $D_{\mathcal{G}}(\ell)$ obtained under random Clifford unitary evolution for the system size $L = 256$.

function of the local Hilbert space dimension. Following the trend of Fig. 5.6, increasing q causes the distribution to sharpen, asymptotically approaching a Dirac delta function centered at $L/2$ in the large-q limit, shown in Fig. 5.7.
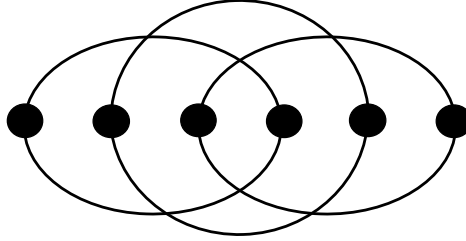
Figure 5.7: Maximally entangled 6-qudit state in the clipped-gauge representation shows each stabilizer thermalizes to length $L/2$.

Chapter 6

Conclusions

6.1 Summary of results

In this thesis, we have investigated measurement-induced entanglement scaling transitions in random quantum circuits composed of prime-dimensional qudits. Following the brickwork unitary circuit model with interspersed local projective measurements studied in Ref. [29], we implemented simulations using the stabilizer formalism extended to prime-dimensional systems. These simulations employed two-qudit Clifford unitaries and computational basis measurements, enabling efficient and scalable numerical simulations.

Our primary finding is that the characteristic features of the entanglement scaling transition observed in qubit systems persist in qudit systems. Specifically, we observe that increasing the rate of local measurements drives the steady-state entanglement entropy from a volume-law to an area-law phase, independent of the local Hilbert space dimension q. However, the critical measurement rate p_c increases convergently with q, approaching the asymptotic value $p_c = 1/2$ as $q \to \infty$ (Fig. 6.1), consistent with existing literature [32].
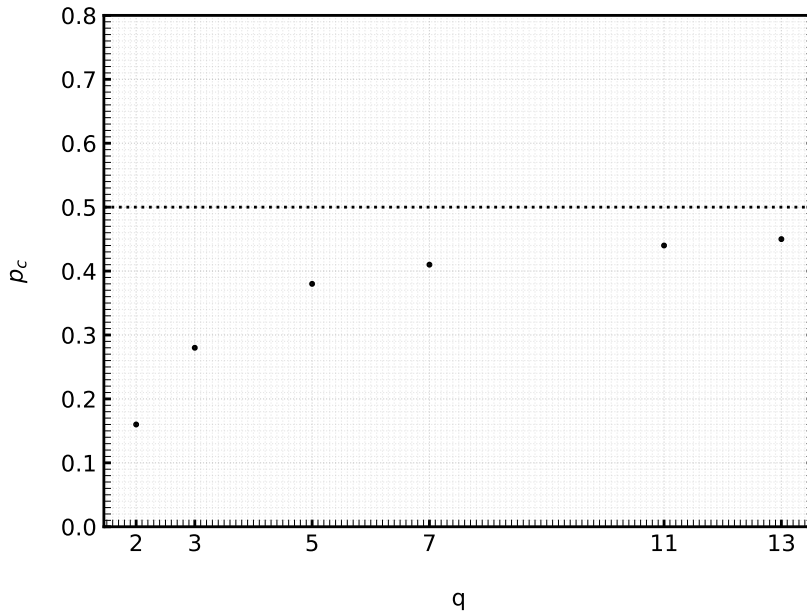
Figure 6.1: Asymptotic convergence of critical measurement rates to $p_c = 1/2$ with increasing local Hilbert space dimension.

Further, the correlation length critical exponent ν, found to be approximately $\nu \approx 1.3$ in qubit systems [29], remains consistent across higher qudit dimensions. This invariance is expected, as the entanglement transition maps to two-dimensional bond percolation in

the $q \to \infty$ limit, which is characterized by $\nu = 4/3$. Nevertheless, complementary work in Ref. [38] investigates additional scaling exponents by analyzing entanglement measures across varying bipartition sizes, at criticality. Their results indicate that critical exponents vary with q, suggesting that each prime-dimensional Hilbert space exhibits a distinct universality class when more nuanced entanglement measures are considered.

In the absence of measurements, we recover entanglement dynamics governed by the Kardar-Parisi-Zhang (KPZ) universality class [76]. The velocity of entanglement spreading increases with q, mirroring the convergent behavior observed at the critical measurement rate. To further understand the large-q regime, we introduced an effective classical dynamical model that captures the impact of Clifford unitary operations without requiring explicit knowledge of their action. This model preserves the essential features of entanglement spreading and becomes exact in the limit $q \to \infty$. This Clifford model replicates the entanglement dynamics described by the surface growth model for Haar-random circuits of Ref. [76], indicating a convergence of the actions of the unitary groups in the large-q limit. In addition to capturing the global surface growth features, it also provides additional insight into the internal structure of entanglement across the lattice. In this regime, we find that all stabilizers attaining a steady state length of $L/2$ is indicative of thermalization, or the complete scrambling of quantum information.

6.2 Outlook

Several interesting directions emerge from the findings and numerical framework presented in this thesis. These include:

Measurements and disentangling unitaries in the classical limit
The natural extension of the clipped-gauge graph-based model introduced in Chapter 5, is the incorporation of measurements, in the limit $q \to \infty$. For small system sizes, integrating measurements is relatively straightforward. A local projective measurement collapses a stabilizer into a loop with support on a single qudit. However, the post-measurement state violates the clipped-gauge conditions, as one stabilizer is abruptly truncated. Consequently, a reclipping procedure is required to restore the system to a valid configuration. At larger system sizes, reclipping becomes significantly more complex, as it requires identifying clusters of qudits that are supported by a linearly independent subset of short-range stabilizer generators, yet are spatially embedded within the support of long-range stabilizers. Since the contents of stabilizers are not explicitly tracked in our classical model, performing this identification is non-trivial. Our ongoing work focuses on designing efficient reclipping rules by analyzing the behavior of unclipped stabilizers in low-dimensional Hilbert spaces. Simultaneously, we plan to explore heuristic models for measurements, including generalizations of the surface growth model introduced in Ref. [76], which may offer computationally tractable alternatives for simulating measurement dynamics. Following the work of Ref. [34], another avenue within this model is to identify the sparse set of *disentangling unitaries*, which can deterministically reduce entanglement at a two-qudit bond by one or half an unit. This addition will permit the study of the unitary-only entanglement transition driven by local disentanglement, as opposed to projective measurements which have nonlocal effects.

Characterization of multipartite entanglement in $q \geq 2$
In a recent work, Ref. [72], the nature of multipartite entanglement in monitored Clifford circuits for the $q = 2$ case was investigated, using the quantum Fisher information as a wit-

ness. Their findings show that *genuine* extensive multipartite entanglement does not arise in the qubit setting regardless of measurement rate, i.e, entanglement is typically restricted to pairs of qubits. Moreover, extensive multipartite entanglement only arises when conservation laws are imposed on the unitary operations. Our analysis indicates that for $q \geq 3$, support-broadening Clifford unitaries become dominant in proportion, leading to a higher likelihood of a set of linearly independent stabilizers supporting a substantial cluster of qudits. Specifically, this results in fewer independently-supported clusters overall, while each cluster encompasses more qudits. A natural question for future investigation is whether this tendency towards extended stabilizer support in higher-dimensional Hilbert spaces correlates with the emergence of genuine multipartite entanglement in the presence of measurements.

MIPTs in composite dimensional Hilbert spaces
This work has focused on prime-dimensional local Hilbert spaces. While the behavior of monitored Clifford systems with prime-power dimensions (q^m) has been explored [38], and shown to exhibit a convergent trend in the critical measurement rate (Fig. 6.1), the case of composite-dimensional Hilbert spaces remains largely unexplored. However, recent generalizations of the stabilizer formalism to arbitrary finite dimensions [107, 120] now enable a systematic extension of our methods to composite systems. An investigation into the entanglement scaling transition in such systems, exploring the trends in critical measurement rates and universal exponents, would be of great interest. While a convergence towards $p_c = 1/2$ is expected in the limit $q \to \infty$, the behavior of critical measurement rates in finite composite dimensions remains an open question.

Measurement-induced topological order in $q \geq 2$
Recent studies have demonstrated that measurement-induced topologically ordered phases can be realized in random circuits using carefully designed joint-qubit measurements [36, 121]. Extending this line of research to qudit systems presents another interesting line of inquiry, as higher local Hilbert space dimensions offer a richer playground to explore stable realizations of topological orders and joint measurement protocols.

Appendix A

Cardinality of the Clifford group

This appendix explores the structure of the Clifford group as a means to deepen the understanding of the numerical framework discussed in Chapter 3. We begin by reviewing the structure of the qubit Clifford group, $\mathrm{Cl}(2, L)$, and extend the discussion to prime-dimensional local Hilbert spaces. Note that this structure is not directly used in our protocol for sampling Clifford elements, presented in the subsequent appendix.

The projective Clifford group, $\overline{\mathrm{Cl}}(q, L) = \mathrm{Cl}(q, L)/\mathrm{U}(1)$, introduced in Chapter 3, is a finite group that normalizes the similarly discretized projective Pauli group, $\overline{\mathcal{P}}(q, L) = \mathcal{P}(q, L)/\mathrm{U}(1)$. In the qubit case, the projective Clifford group exhibits the well-known exponential scaling of its cardinality [114, 122]:

$$\left| \overline{\mathrm{Cl}}(2, \mathrm{L}) \right| = 2^{L^2 + 2L} \prod_{j=1}^{L} (4^j - 1). \tag{A.1}$$

In odd-prime dimensions, the projective Clifford group exhibits a symplectic substructure, given by the quotient relation [123]:

$$\overline{\mathrm{Cl}}(q, L)/\overline{\mathcal{P}}(q, L) \cong \mathrm{Sp}(q, 2L), \tag{A.2}$$

where $\mathrm{Sp}(q, 2L)$ denotes the symplectic group, consisting of matrices over the finite field $\mathbb{F}_q$ that satisfy the condition:

$$\mathrm{Sp}(q, 2L) = \{M \,|\, M^T J M = J\}, \quad \text{where} \quad J = \begin{bmatrix} 0 & I_L \\ -I_L & 0 \end{bmatrix}. \tag{A.3}$$

The cardinality of the symplectic group is given by [99]:

$$|\mathrm{Sp}(q, 2L)| = q^{L^2} \prod_{j=1}^{L} (q^{2j} - 1). \tag{A.4}$$

Upon substituting this cardinality into the equivalence relation of the Clifford substructure Eq. A.2, the cardinality of the odd-prime dimensional Clifford group becomes:

$$\left| \overline{\mathrm{Cl}}(q, L) \right| = \left| \overline{\mathcal{P}}(q, L) \right| \cdot |\mathrm{Sp}(q, 2L)|, \tag{A.5}$$

$$= q^{L^2 + 2L} \prod_{j=1}^{L} (q^{2j} - 1). \tag{A.6}$$

Hence, in prime dimensional Hilbert spaces, the projective Clifford group exhibits exponential scaling of order $O(q^{L^2})$. Previous analytical studies have formalized this scaling for both prime [124] and composite-dimensional [125] single-qudit projective Clifford groups. Further, the recent work of Ref. [99] presents a rigorous derivation of the Clifford cardinality

and structure in arbitrary composite dimensions.

As discussed in Chapter 3, the simulation of entanglement scaling transitions does not require tracking the global phases on the generalized Pauli operator, which generally ensure the completeness of the group. Consequently, the number of elements in the Clifford group is reduced. Specifically, the cardinality of the Clifford group equals that of the symplectic group, described in Eq. A.4.

Appendix B

Generation of random Clifford unitaries

In addition to the stabilizer tableau representation used in this work, Clifford circuits can also be simulated using graph state representations, affine representations, or variants of the stabilizer tableau itself [91]. Regardless of the chosen representation, the cardinality of the Clifford group scales exponentially with the local Hilbert space dimension, as discussed in Appendix A. This exponential growth presents a significant challenge for uniform and efficient sampling of random unitaries from the Clifford group.

Several approaches have been developed to address this challenge. Ref. [114] exploits the symplectic substructure of the qubit Clifford group to index individual elements, providing a uniform sampling algorithm with an $O(N^3)$ scaling. Refs. [111] and [122] leverage the characteristic actions of the qubit Clifford group generators on the stabilizer tableau, for $O(N^2)$ scaling algorithms which construct random Clifford elements. Ref. [112] utilizes the so-called Bruhat decomposition to define a canonical form for qubit Clifford group elements, and outlines a uniform sampling algorithm with $O(N^2)$ scaling as well.

In particular, the *tableau algorithm* proposed in Ref. [111] details an efficient numerical implementation of the qubit Clifford group generators: the CNOT (CX), Hadamard (H), and phase (P) gates, thereby playing a foundational role in the efficient simulations of qubit Clifford circuits [94]. While individual Clifford group elements can be obtained by randomly sequencing these generators, ensuring uniformity in this sampling process is not straight forward.

An intuitive approach to ensure uniform distribution could be the generation of the complete 2-qudit Clifford group $(\mathrm{Cl}(q, 2))$, followed by the sampling of individual elements. This can be carried out systemically in the stabilizer representation, wherein each Clifford unitary is represented as a set of unitary maps, for pairs of single-qudit Pauli generators. The commutation relations between these unitary maps facilitate the systematic construction of the Clifford group [29].

However, at higher local Hilbert space dimensions, the exponential growth in the group's cardinality prohibits the generation of the complete group. Hence, in this work, we utilize this method to generate individual Clifford group elements on-the-fly, while ensuring a uniform sampling distribution. Below, we detail this implementation in Python. Herein, we employ the Python `itertools` library, as iterators are a memory-efficient alternative to storing large arrays of group elements.

```python
1    """ python library imports """
2    import numpy as np
3    import itertools as it
4
5    def commutator(ps1, ps2, qdim):
```

```
6              """
7              Symplectic inner - product that returns the commutator
8              between two N-qudit pauli strings (ps1 , ps2)
9              """
10             N = len(ps1)//2
11             return (ps1[N:2*N]@ ps2[:N]-ps1[:N]@ps2[N:2*N])%qdim
```

The pair of single-qudit Pauli group generators, $X_{\mathsf{q}}^{(i)}$ and $Z_{\mathsf{q}}^{(i)}$, form a complete basis on qudit i, and satisfy the commutation relation $[X_{\mathsf{q}}^{(i)}, Z_{\mathsf{q}}^{(j)}] = (q-1) \cdot \delta_{ij}$. As a prerequisite to the sampling algorithm, we identify all pairs of Pauli strings that maximally anticommute, for 1-qudit and 2-qudit Pauli strings.

```
12        def generate_anticomm_set(qdim , nqudits):
13             """
14             Parameters
15             ----------
16             qdim : local Hilbert space dimension
17             nqudits : length of Pauli string
18             """
19
20             # filtering function
21             acomm = lambda xz: commutator(xz[0], xz[1], qdim) == (qdim -1)
22
23             # identify all pairs
24             xz_pairs = list(it.product(list(it.product(list(range(qdim)), repeat
        = 2*nqudits))[1:], repeat = 2))
25
26             # filter anticommuting pairs
27             xz_anti = list(filter(acomm , xzcombs))
28             return xz_anti
```

The set of maximally anticommuting single-qudit Pauli strings constitutes the single-qudit Clifford group $(\mathrm{Cl}(q, 1))$. Herein, each element represented as unitary maps for single-qudit Pauli generators $X_{\mathsf{q}}^{(1)}$ and $Z_{\mathsf{q}}^{(1)}$. These two sets of maximally anticommuting Pauli strings serve as arguments for the 4-stage random Clifford sampling algorithm described below:

```
29        def random_cliff_dynamic(qdim , xz_anti_1 , xz_anti_2):
30             """
31                 Function to sample random Cl(qdim , n=2) element.\\
32                 Parameters
33                 ----------
34                 qdim : local Hilbert space dimension
35                 xz_anti_1 : Clifford group Cl(qdim , 1)
36                 xz_anti_2 : pairs of 2-qudit anticommuting Pauli strings
37             """
```

1. Maximally anticommuting 2-qudit Pauli strings can be interpreted as a maps for the Pauli generators of either the first qudit $(X_{\mathsf{q}}I, Z_{\mathsf{q}}I)$, or the second qudit $(IX_{\mathsf{q}}, IZ_{\mathsf{q}})$. We begin by uniformly sampling one anticommuting pair and the evaluate its local commutators. These commutators determine its interpretation as a mapping for the Pauli generators for either the first or second qudit. Here, for illustration, we presume the sampled pair represents a mapping on the first qudit, and denote it $(X_{(1)}, Z_{(1)})$.

```
38              # sample 2-qudit anticomm. pair
39              num_xz_anti_2 = len(xz_anti_2)
40              Xn, Zn = xz_anti_2[np.random.choice(num_xz_anti_2)]
41
42              # Identify local anti-commutation
43              for i in range(2):
44                  if not commutator([Xn[i],Xn[i+2]],[Zn[i],Zn[i+2]], qdim) == 0:
45                      first_anti = i
46                      break
47
48              # Initialize a blank Clifford unitary
49              # Xtrans contains maps for IX, XI
50              # Ztrans contains maps for IZ, ZI
51              Xtrans, Ztrans = np.identity(4, dtype = int).reshape(2,2,4)
52
53              # Re-arrange rows for further steps
54              Xtrans[first_anti] = Xn
55              Ztrans[first_anti] = Zn
56
57              Xtrans[[0, first_anti]] = Xtrans[[first_anti, 0]]
58              Ztrans[[0, first_anti]] = Ztrans[[first_anti, 0]]
```

2. Next, we seek a mapping for the remaining two Pauli generators $(X_{(2)}, Z_{(2)})$. Without loss of generality, we begin by constructing the $Z_{(2)}$ generator, such that it commutes with the two existing maps. This construction relies on the cyclical nature of the commutation relations in the N-qudit Pauli group. Particularly, as $[X_{(1)}, Z_{(1)}] \neq 0$, we can construct $\tilde{Z}_{(2)} = Z_{(1)}^\alpha X_{(1)}^\beta Z_{(2)}$ such that $[X_{(1)}, \tilde{Z}_{(2)}] = 0$ and $[Z_{(1)}, \tilde{Z}_{(2)}] = 0$, where,

$$\alpha = q - [Z_{(2)}, X_{(1)}]$$
$$\beta = [Z_{(2)}, Z_{(1)}]$$
(B.1)

```
60              # ensure that Z1 commutes with X0 and Z0
61              commutator_z1x0 = commutator(Ztrans[1], Xtrans[0], qdim)
62              if commutator_z1x0 != 0:
63                  Ztrans[1] += (qdim - commutator_z1x0) * Ztrans[0]
64                  Ztrans[1] %= qdim
65
66              commutator_z1z0 = commutator(Ztrans[1], Ztrans[0], qdim)
67              if commutator_z1z0 != 0:
68                  Ztrans[1] += commutator_z1z0 * Xtrans[0]
69                  Ztrans[1] %= qdim
```

3. A similar construction follows for $X_{(2)}$. For prime-dimensional local Hilbert spaces, we can determine ϕ such that $[X_{(2)}^\phi, Z_{(2)}] = q - 1$. As before, we ensure that $X_{(2)}$ commutes with $(X_{(1)}, Z_{(1)})$. Hence, we obtain $\tilde{X}_{(2)} = Z_{(1)}^\gamma X_{(1)}^\delta Z_{(2)}^\phi$, where,

$$\gamma = q - [X_{(2)}, X_{(1)}]$$
$$\delta = [X_{(2)}, Z_{(1)}]$$
(B.2)

```
70              temp_x1 = Xtrans[1].copy()
71              while commutator(Xtrans[1], Ztrans[1], qdim) != qdim-1:
72                  Xtrans[1] += temp_x1
73                  Xtrans[1] %= qdim
```

```
74
75          # make sure that X1 commutes with all X0 and Z0
76          commutator_x1x0 = commutator(Xtrans[1], Xtrans[0], qdim)
77          if commutator_x1x0 != 0:
78              Xtrans[1] += (qdim - commutator_x1x0) * Ztrans[0]
79              Xtrans[1] %= qdim
80
81          commutator_x1z0 = commutator(Xtrans[1], Ztrans[0], qdim)
82          if commutator_x1z0 != 0:
83              Xtrans[1] += (commutator_x1z0) * Xtrans[0]
84              Xtrans[1] %= qdim
```

4. Though we have extended the uniformly sampled two-qudit anticommuting pair of Pauli strings to a valid unitary map, it does not yet represent a random element of the complete Clifford group. The complete set of Clifford rotations is obtained upon including single-qudit unitaries in the above transformation [29]. To complete the generation of the individual Clifford element, we uniformly sample a random element of $\mathrm{Cl}(q, 1)$, and multiply it with the constructed two-qudit map.

```
85          # rearrange generator according to basis
86          Xtrans[[0,1]] = Xtrans[[1, 0]]
87          Ztrans[[0,1]] = Ztrans[[1, 0]]
88
89          # Form 2-qudit unitary map
90          U2 = np.concatenate((Xtrans, Ztrans))
91
92          # select 1-qudit Clifford
93          num_xz_anti_1 = len(xz_anti_1)
94          V = xz_anti_1[np.random.choice(num_xz_anti_1)]
95
96          # extend 1-qudit Clifford to a 2-qudits map
97          U1 = np.identity(4, dtype = int)
98          U1[[0], [0,2]] = V[[0]]
99          U1[[2], [0,2]] = V[[1]]
100
101         # return random unitary
102         return (U1@U2)%qdim
```

As we restrict ourselves to two-qudit Cliffords, such an implementation offers a nearly uniform sampling time, regardless of the local Hilbert space dimension. Variations in the sampling time will likely arise based on the integer datatype required for representing matrix multiplications for a given local Hilbert space dimension.

Bibliography

[1] A. Einstein, B. Podolsky, and N. Rosen, Physical review **47**, 777 (1935).

[2] J. S. Bell, Physics Physique Fizika **1**, 195 (1964).

[3] A. Aspect, J. Dalibard, and G. Roger, Physical review letters **49**, 1804 (1982).

[4] B. Hensen, H. Bernien, A. E. Dréau, A. Reiserer, N. Kalb, M. S. Blok, J. Ruitenberg, R. F. Vermeulen, R. N. Schouten, C. Abellán, *et al.*, Nature **526**, 682 (2015).

[5] L. K. Shalm, E. Meyer-Scott, B. G. Christensen, P. Bierhorst, M. A. Wayne, M. J. Stevens, T. Gerrits, S. Glancy, D. R. Hamel, M. S. Allman, *et al.*, Physical review letters **115**, 250402 (2015).

[6] M. Giustina, M. A. Versteegh, S. Wengerowsky, J. Handsteiner, A. Hochrainer, K. Phelan, F. Steinlechner, J. Kofler, J.-Å. Larsson, C. Abellán, *et al.*, Physical review letters **115**, 250401 (2015).

[7] S. Storz, J. Schär, A. Kulikov, P. Magnard, P. Kurpiers, J. Lütolf, T. Walter, A. Copetudo, K. Reuer, A. Akin, *et al.*, Nature **617**, 265 (2023).

[8] P. W. Shor, Physical review A **52**, R2493 (1995).

[9] C. H. Bennett, D. P. DiVincenzo, J. A. Smolin, and W. K. Wootters, Physical Review A **54**, 3824 (1996).

[10] J. Behrends, F. Venn, and B. Béri, Physical Review Research **6**, 013137 (2024).

[11] R. Horodecki, P. Horodecki, M. Horodecki, and K. Horodecki, Reviews of modern physics **81**, 865 (2009).

[12] M. A. Nielsen and I. L. Chuang, *Quantum computation and quantum information* (Cambridge university press, 2010).

[13] A. K. Ekert, Physical review letters **67**, 661 (1991).

[14] V. Giovannetti, S. Lloyd, and L. Maccone, Science **306**, 1330 (2004).

[15] S. F. Huelga, C. Macchiavello, T. Pellizzari, A. K. Ekert, M. B. Plenio, and J. I. Cirac, Physical Review Letters **79**, 3865 (1997).

[16] W. Dür, M. Skotiniotis, F. Froewis, and B. Kraus, Physical Review Letters **112**, 080801 (2014).

[17] P. Calabrese and J. Cardy, Journal of statistical mechanics: theory and experiment **2004**, P06002 (2004).

[18] P. Calabrese and J. Cardy, Journal of physics a: mathematical and theoretical **42**, 504005 (2009).

[19] A. Kitaev and J. Preskill, Physical review letters **96**, 110404 (2006).

[20] H. Li and F. D. M. Haldane, Physical review letters **101**, 010504 (2008).

[21] F. Verstraete, V. Murg, and J. I. Cirac, Advances in physics **57**, 143 (2008).

[22] U. Schollwöck, Annals of physics **326**, 96 (2011).

[23] M. B. Hastings, Physical Review B-Condensed Matter and Materials Physics **76**, 035114 (2007).

[24] G. Vidal, Physical review letters **91**, 147902 (2003).

[25] F. Verstraete and J. I. Cirac, Physical Review B-Condensed Matter and Materials Physics **73**, 094423 (2006).

[26] D. A. Abanin, E. Altman, I. Bloch, and M. Serbyn, Reviews of Modern Physics **91**, 021001 (2019).

[27] J. H. Bardarson, F. Pollmann, and J. E. Moore, Physical review letters **109**, 017202 (2012).

[28] M. P. Fisher, V. Khemani, A. Nahum, and S. Vijay, Annual Review of Condensed Matter Physics **14**, 335 (2023).

[29] Y. Li, X. Chen, and M. P. Fisher, Physical Review B **100**, 134306 (2019).

[30] F. Arute, K. Arya, R. Babbush, D. Bacon, J. C. Bardin, R. Barends, R. Biswas, S. Boixo, F. G. Brandao, D. A. Buell, *et al.*, Nature **574**, 505 (2019).

[31] C.-M. Jian, Y.-Z. You, R. Vasseur, and A. W. Ludwig, Physical Review B **101**, 104302 (2020).

[32] Y. Bao, S. Choi, and E. Altman, Physical Review B **101**, 104301 (2020).

[33] M. Ippoliti, M. J. Gullans, S. Gopalakrishnan, D. A. Huse, and V. Khemani, Physical Review X **11**, 011030 (2021).

[34] R. Morral-Yepes, A. Smith, S. L. Sondhi, and F. Pollmann, PRX Quantum **5**, 010309 (2024).

[35] A. Lavasani, Y. Alavirad, and M. Barkeshli, Physical review letters **127**, 235701 (2021).

[36] A. Lavasani, Y. Alavirad, and M. Barkeshli, Nature Physics **17**, 342 (2021).

[37] J. W. Merritt, *Measurement-Induced Quantum Phase Transitions*, Ph.D. thesis, University of Washington (2023).

[38] Y. Li, R. Vasseur, M. P. Fisher, and A. W. Ludwig, Physical Review B **109**, 174307 (2024).

[39] X. Yu and X.-L. Qi, arXiv preprint arXiv:2201.12704 (2022).

[40] R. Fan, S. Vijay, A. Vishwanath, and Y.-Z. You, Physical Review B **103**, 174309 (2021).

[41] Z. Weinstein, Y. Bao, and E. Altman, Physical Review Letters **129**, 080501 (2022).

[42] Z.-C. Yang, Y. Li, M. P. Fisher, and X. Chen, Physical Review B **105**, 104306 (2022).

[43] H. Liu, T. Zhou, and X. Chen, Physical Review B **106**, 144311 (2022).

[44] D. Gottesman, in *NASA International Conference on Quantum Computing and Quantum Communications* (Springer, 1998) pp. 302–313.

[45] Y. Wang, Z. Hu, B. C. Sanders, and S. Kais, Frontiers in Physics **8**, 589504 (2020).

[46] E. T. Campbell, Physical review letters **113**, 230501 (2014).

[47] D. Cozzolino, B. Da Lio, D. Bacco, and L. K. Oxenløwe, Advanced Quantum Technologies **2**, 1900038 (2019).

[48] P. J. Ollitrault, G. Mazzola, and I. Tavernelli, Physical Review Letters **125**, 260511 (2020).

[49] B. Bauer, S. Bravyi, M. Motta, and G. K.-L. Chan, Chemical reviews **120**, 12685 (2020).

[50] B. P. Lanyon, J. D. Whitfield, G. G. Gillett, M. E. Goggin, M. P. Almeida, I. Kassal, J. D. Biamonte, M. Mohseni, B. J. Powell, M. Barbieri, *et al.*, Nature chemistry **2**, 106 (2010).

[51] S. V. Mathis, G. Mazzola, and I. Tavernelli, Physical Review D **102**, 094501 (2020).

[52] Y. Deller, S. Schmitt, M. Lewenstein, S. Lenk, M. Federer, F. Jendrzejewski, P. Hauke, and V. Kasper, Physical Review A **107**, 062410 (2023).

[53] B. P. Lanyon, M. Barbieri, M. P. Almeida, T. Jennewein, T. C. Ralph, K. J. Resch, G. J. Pryde, J. L. OâĂŹbrien, A. Gilchrist, and A. G. White, Nature Physics **5**, 134 (2009).

[54] L. E. Fischer, D. Miller, F. Tacchino, P. K. Barkoutsos, D. J. Egger, and I. Tavernelli, Physical review research **4**, 033027 (2022).

[55] A. S. Nikolaeva, E. O. Kiktenko, and A. K. Fedorov, EPJ Quantum Technology **11**, 1 (2024).

[56] D. Gottesman, A. Kitaev, and J. Preskill, Physical Review A **64**, 012310 (2001).

[57] M. H. Michael, M. Silveri, R. Brierley, V. V. Albert, J. Salmilehto, L. Jiang, and S. M. Girvin, Physical Review X **6**, 031006 (2016).

[58] C. Cafaro, F. Maiolini, and S. Mancini, Physical Review AâĂŤAtomic, Molecular, and Optical Physics **86**, 022308 (2012).

[59] M. Ringbauer, M. Meth, L. Postler, R. Stricker, R. Blatt, P. Schindler, and T. Monz, Nature Physics **18**, 1053 (2022).

[60] D. González-Cuadra, T. V. Zache, J. Carrasco, B. Kraus, and P. Zoller, Physical Review Letters **129**, 160501 (2022).

[61] L. E. Fischer, A. Chiesa, F. Tacchino, D. J. Egger, S. Carretta, and I. Tavernelli, PRX Quantum **4**, 030327 (2023).

[62] H. J. Briegel, D. E. Browne, W. Dür, R. Raussendorf, and M. Van den Nest, Nature Physics **5**, 19 (2009).

[63] D. P. DiVincenzo, D. W. Leung, and B. M. Terhal, IEEE Transactions on Information Theory **48**, 580 (2002).

[64] J. Eisert, M. Cramer, and M. B. Plenio, Reviews of modern physics **82**, 277 (2010).

[65] G. Vidal, Journal of Modern Optics **47**, 355 (2000).

[66] R. Islam, R. Ma, P. M. Preiss, M. Eric Tai, A. Lukin, M. Rispoli, and M. Greiner, Nature **528**, 77 (2015).

[67] A. M. Kaufman, M. E. Tai, A. Lukin, M. Rispoli, R. Schittko, P. M. Preiss, and M. Greiner, Science **353**, 794 (2016).

[68] V. Vitale, A. Elben, R. Kueng, A. Neven, J. Carrasco, B. Kraus, P. Zoller, P. Calabrese, B. Vermersch, and M. Dalmonte, SciPost Physics **12**, 106 (2022).

[69] M. B. Hastings, I. González, A. B. Kallin, and R. G. Melko, Physical review letters **104**, 157201 (2010).

[70] M. M. Wolf, F. Verstraete, M. B. Hastings, and J. I. Cirac, Physical review letters **100**, 070502 (2008).

[71] G. De Tomasi, S. Bera, J. H. Bardarson, and F. Pollmann, Physical Review Letters **118**, 016804 (2017).

[72] A. Lira-Solanilla, X. Turkeshi, and S. Pappalardi, arXiv preprint arXiv:2412.16062 (2024).

[73] M. B. Hastings, Journal of statistical mechanics: theory and experiment **2007**, P08024 (2007).

[74] B. Bauer and C. Nayak, Journal of Statistical Mechanics: Theory and Experiment **2013**, P09005 (2013).

[75] G. Vidal, Physical review letters **93**, 040502 (2004).

[76] A. Nahum, J. Ruhman, S. Vijay, and J. Haah, Physical Review X **7**, 031016 (2017).

[77] M. Kardar, G. Parisi, and Y.-C. Zhang, Physical Review Letters **56**, 889 (1986).

[78] R. Oliveira, O. Dahlsten, and M. Plenio, Physical review letters **98**, 130502 (2007).

[79] Y. Li, X. Chen, and M. P. Fisher, Physical Review B **98**, 205136 (2018).

[80] M. Ippoliti and V. Khemani, Physical Review Letters **126**, 060501 (2021).

[81] G. Q. AI, Nature **622**, 481 (2023).

[82] J. M. Koh, S.-N. Sun, M. Motta, and A. J. Minnich, Nature Physics **19**, 1314 (2023).

[83] C. Noel, P. Niroula, D. Zhu, A. Risinger, L. Egan, D. Biswas, M. Cetina, A. V. Gorshkov, M. J. Gullans, D. A. Huse, *et al.*, Nature Physics **18**, 760 (2022).

[84] M. J. Gullans and D. A. Huse, Physical Review X **10**, 041020 (2020).

[85] Y. Li, Y. Zou, P. Glorioso, E. Altman, and M. P. Fisher, Physical Review Letters **130**, 220404 (2023).

[86] S. J. Garratt and E. Altman, PRX Quantum **5**, 030311 (2024).

[87] H. Kamakari, J. Sun, Y. Li, J. J. Thio, T. P. Gujarati, M. P. Fisher, M. Motta, and A. J. Minnich, Physical Review Letters **134**, 120401 (2025).

[88] X. Feng, J. Côté, S. Kourtis, and B. Skinner, arXiv preprint arXiv:2502.01735 (2025).

[89] D. Gottesman, *Stabilizer codes and quantum error correction* (California Institute of Technology, 1997).

[90] D. Gottesman, arXiv preprint quant-ph/9807006 (1998).

[91] A. Kerzner, *Clifford simulation: Techniques and applications*, Master's thesis, University of Waterloo (2021).

[92] S. Anders and H. J. Briegel, Physical Review AâĂŤAtomic, Molecular, and Optical Physics **73**, 022334 (2006).

[93] M. Nest, arXiv preprint arXiv:0811.0898 (2008).

[94] C. Gidney, Quantum **5**, 497 (2021).

[95] R. Raussendorf and H. J. Briegel, Physical review letters **86**, 5188 (2001).

[96] R. Raussendorf, International Journal of Quantum Information **7**, 1053 (2009).

[97] E. Onorati, A. Werner, and J. Eisert, Physical review letters **123**, 060501 (2019).

[98] J. J. Wallman, Quantum **2**, 47 (2018).

[99] M. Heinrich, *On stabiliser techniques and their application to simulation and certification of quantum devices*, Ph.D. thesis, Universität zu Köln (2021).

[100] C. Dankert, R. Cleve, J. Emerson, and E. Livine, Physical Review AâĂŤAtomic, Molecular, and Optical Physics **80**, 012304 (2009).

[101] S. Bravyi and D. Gosset, Physical review letters **116**, 250501 (2016).

[102] T. Haug and L. Piroli, Physical Review B **107**, 035148 (2023).

[103] P. S. Tarabunga, E. Tirrito, M. C. Bañuls, and M. Dalmonte, Physical Review Letters **133**, 010601 (2024).

[104] M. Bejan, C. McLauchlan, and B. Béri, PRX Quantum **5**, 030332 (2024).

[105] M. Jafarzadeh, Y.-D. Wu, Y. R. Sanders, and B. C. Sanders, New Journal of Physics **22**, 063014 (2020).

[106] D. Amaro-Alcalá, B. C. Sanders, and H. de Guise, New Journal of Physics **26**, 073052 (2024).

[107] E. Hostens, J. Dehaene, and B. De Moor, Physical Review A-Atomic, Molecular, and Optical Physics **71**, 042315 (2005).

[108] R. A. Bertlmann and P. Krammer, Journal of Physics A: Mathematical and Theoretical **41**, 235303 (2008).

[109] E. Knill, arXiv preprint quant-ph/9608049 (1996).

[110] T. Santhanam and A. Tekumalla, Foundations of Physics **6**, 583 (1976).

[111] S. Aaronson and D. Gottesman, Physical Review A - Atomic, Molecular, and Optical Physics **70**, 052328 (2004).

[112] S. Bravyi and D. Maslov, IEEE Transactions on Information Theory **67**, 4546 (2021).

[113] T. Itoko and R. Raymond, in *2021 IEEE International Conference on Quantum Computing and Engineering (QCE)* (IEEE, 2021) pp. 188–198.

[114] R. Koenig and J. A. Smolin, Journal of Mathematical Physics **55** (2014).

[115] D. Gross, Journal of mathematical physics **47** (2006).

[116] M. M. Wilde, *Quantum information theory* (Cambridge university press, 2013).

[117] B. Skinner, J. Ruhman, and A. Nahum, Physical Review X **9**, 031009 (2019).

[118] A. C. Potter and R. Vasseur, in *Entanglement in Spin Chains: From Theory to Quantum Technology Applications* (Springer, 2022) pp. 211–249.

[119] R. Vasseur, A. C. Potter, Y.-Z. You, and A. W. Ludwig, Physical Review B **100**, 134203 (2019).

[120] É. Descamps and B. Dakić, Journal of Physics A: Mathematical and Theoretical **57**, 455301 (2024).

[121] R. Morral-Yepes, F. Pollmann, and I. Lovas, Physical Review B **108**, 224304 (2023).

[122] E. Van Den Berg, in *2021 ieee international conference on quantum computing and engineering (qce)* (IEEE, 2021) pp. 54–59.

[123] G. Nebe, E. M. Rains, and N. J. Sloane, Designs, Codes and Cryptography **24**, 99 (2001).

[124] D. M. Appleby, Journal of Mathematical Physics **46** (2005).

[125] J. Tolar, in *Journal of Physics: Conference Series*, Vol. 1071 (IOP Publishing, 2018) p. 012022.

List of Figures

List of Tables

Acknowledgements

Finally, I would like to acknowledge and express my gratitude to those who made this thesis possible.

I am sincerely grateful to Prof. Frank Pollmann for the opportunity to explore a new research direction for my master's thesis - a project I have thoroughly enjoyed. His guidance in framing and refocusing the work at crucial junctures was key to its progress. Above all, his advice, support, and consistently positive and lively outlook on both this research, and academic life more broadly, has been a constant source of motivation and encouragement. I am truly thankful for his mentorship.

My deepest gratitude goes to my direct supervisor, Raúl Morral-Yepes, for his constant support and steady enthusiasm throughout this project. His abundance of interesting ideas, and further willingness to collaborate and brainstorm, has made the experience both smooth and enjoyable. I also deeply appreciate his detailed feedback, which significantly contributed to the clarity and quality of this thesis.

I am thankful for the companionship and motivation provided by my fellow students, both master's and doctoral, at the Condensed Matter Theory chair: Luis, Lukas, Lukas, Lorenzo, Adam, Marc, Markus, and Fabian. Their support during summer schools, conferences, hikes, and dinners has been a truly enriching part of the past year. Their welcoming natures and inquisitive dispositions continue to be a source of inspiration.

Above all, I sincerely appreciate all those who took the time to share their work with me and took interest in mine. These exchanges sparked my curiosity in directions I now hope to explore further, pushed me to scrutinize my work more carefully.

Lastly, I am deeply grateful to my parents, for their unwavering support and belief, which have made it possible for me to journey from the arts and engineering into physics. Special thanks go to my cohort: Saniya, Pablo, Ka Hui, Diego, Hamzah, and Umut, for support and companionship over the past year.